Analytical Methods

Enhanced characterization of breast cancer phenotypes using Raman micro-spectroscopy on stainless steel substrate.

Journal:	*Analytical Methods*
Manuscript ID	AY-ART-10-2022-001764.R1
Article Type:	Paper
Date Submitted by the Author:	06-Feb-2023
Complete List of Authors:	Thomas, Giju; Vanderbilt University, Biomedical Engineering Fitzgerald, Sean; Vanderbilt University, Biomedical Engineering Gautam, Rekha ; Tyndall National Institute Chen, Fuyao; Yale School of Medicine Haugen, Ezekiel; Vanderbilt University, Biomedical Engineering Rasiah, Pratheepa; Vanderbilt University, Biomedical Engineering Adams, Wilson; Vanderbilt University, Biomedical Engineering Mahadevan-Jansen, Anita; Vanderbilt University, Biomedical Engineering

Enhanced characterization of breast cancer phenotypes using Raman micro-spectroscopy on stainless steel substrate.

Giju Thomas[1,2], Sean T. Fitzgerald[1,2], Rekha Gautam[3], Fuyao Chen[4], Ezekiel Haugen[1,2], Pratheepa K. Rasiah[1,2], Wilson R. Adams[5], and Anita Mahadevan-Jansen[1,2*]

[1]Vanderbilt Biophotonics Center, Vanderbilt University, Nashville, TN 37235, USA

[2]Department of Biomedical Engineering, Vanderbilt University, Nashville, TN 37235, USA

[3]Tyndall National Institute, Cork, T12 R5CP, Ireland

[4]Yale School of Medicine, Yale University, New Haven, CT 06510, USA

[5]Department of Pharmacology, Vanderbilt University, Nashville, TN 37232, USA

*Corresponding author: anita.mahadevan-jansen@vanderbilt.edu

Abstract: Biochemical insights into varying breast cancer (BC) phenotypes can provide a fundamental understanding of BC pathogenesis, while identifying novel therapeutic targets. Raman spectroscopy (RS) can gauge these biochemical differences with high specificity. For routine RS, cells are traditionally seeded onto calcium fluoride (CaF_2) substrates that are costly and fragile, limiting its widespread adoption. Stainless steel has been interrogated previously as a less expensive alternative to CaF_2 substrates, while reporting increased Raman signal intensity than the latter. We sought to further investigate and compare the Raman signal quality measured from stainless steel versus CaF_2 substrates by characterizing different BC phenotypes with altered human epidermal growth factor receptor 2 (HER2) expression.

Raman spectra were obtained on stainless steel and CaF_2 substrates for HER2-negative cells – MDA-MB-231, MDA-MB-468 and HER2-overexpressing cells – AU565, SKBr3. Upon analyzing signal-to-noise ratios (SNR), stainless steel provided a stronger Raman signal, improving SNR by 119% at 1450 cm^{-1} and 122% at 2925 cm^{-1} on average compared to the CaF_2 substrate.

Utilizing only 22% of laser power on sample relative to the CaF_2 substrate, stainless steel still yielded improved spectral characterization over CaF_2, achieving 96.0% versus 89.8% accuracy in BC phenotype discrimination and equivalent 100.0% accuracy in HER2 status classification. Spectral analysis further highlighted increased lipogenesis and altered metabolism in HER2-overexpressing cells, which was subsequently visualized with coherent anti-Stokes Raman scattering microscopy.

Our findings demonstrate that stainless steel substrates deliver improved Raman signal and enhanced spectral characterization, underscoring its potential as a cost-effective alternative to CaF_2 for non-invasively monitoring cellular biochemical dynamics in translational cancer research.

Keywords: *breast cancer, Raman spectroscopy, stainless-steel, signal-to-noise ratio, human epidermal growth factor, cancer phenotype, cancer metabolism*

Introduction

In 2022, an estimated 287,850 new cases of invasive breast cancer (BC) would have been diagnosed in the US[1], with BC mortality poised to remain the second leading cause of cancer death among American women.[2] In recent decades, significant progress has been made toward understanding the mechanism of BC progression, which has led to the development of innovative therapies for countering BC progression and mortality. To develop more effective BC therapies that can optimally offset toxicity and potential cancer resistance, it becomes pivotal to gain a vital understanding of the dynamics that occur at a molecular level in BC.[3-9] The subtle biochemical alterations in BC that may predispose to tumor aggressiveness, propensity for metastasis or drug resistance can be readily studied with Raman spectroscopy, which has been demonstrated to be sensitive to changes in cellular/tissue biochemistry during carcinogenesis.[10-15] Raman spectroscopy is a non-invasive optical technique that relies on detecting photons that inelastically scatter in a unique manner for each molecular bond, making it an ideal modality to probe cell or tissue biochemistry as each biological molecule will possess a distinct Raman spectrum. As a

result, Raman spectroscopy is capable of generating abundant spectral information pertaining to biochemical composition of various cancer cell-lines or tissues, including those of BC.[16-22] Among the different phenotypes, BC with overexpression of human epidermal growth factor receptor-2 (i.e., HER2+) tend to multiply and spread faster than HER2- BC, but is highly responsive to HER2 receptor antagonists. In contrast, triple-negative breast cancer (TNBC) lacks all three receptors for estrogen, progesterone and HER2, making TNBCs also a very aggressive form of HER2- BC phenotype that has poor prognosis and is extremely difficult to treat. The scope of Raman spectroscopy has been established previously to discriminate between biochemical compositions and microenvironments of different BC phenotypes.[22-26] Raman spectroscopy would therefore be able to provide crucial insights on the biochemical mechanisms that drives cancer survival and invasiveness in aggressive BC that carry poor prognosis, particularly for TNBC/HER2- and HER2+ phenotypes.

To study cancer cell-lines or tissues with Raman spectroscopy, the biological samples are usually mounted on a variety of substrates - calcium fluoride (CaF_2), aluminum, quartz and 3D collagen gels – for spectral collection.[27] As such, when selecting a substrate to support the biological materials during spectral acquisition, it becomes imperative that the substrate contributes negligible Raman background noise so as to not obscure relevant Raman spectral information arising from the cells/tissues.[27] Currently, CaF_2 substrates are the most widely used substrates in Raman spectroscopy as they provide low Raman background signal and high optical transmission. However, CaF_2 and other substrate materials that produce minimal Raman background are often expensive.[27] CaF_2 substrates are further disadvantaged by their fragile and brittle nature, which limits their sustainability and implementation in routine clinical settings.[28] Finding more sturdy and cost-effective biocompatible substrates with negligible Raman background noise is therefore pivotal to expanding the latent potential of Raman spectroscopy in contemporary settings for clinical and translational cancer research. In addition, the substrate

should ideally yield excellent Raman signal-to-noise ratios (SNR) and spatial resolution without requiring high laser powers or long exposure times, despite the inherently weak nature of Raman signals from biological materials.

Employing surface-enhanced Raman scattering to amplify Raman signal intensity through the use of silver or gold nanoparticle-coated substrates, which exhibit surface plasmon resonances, has been widely reported.[29, 30] However, this approach adds considerable costs to substrate manufacturing. Kerr *et al.* first noted a considerably stronger Raman signal from human cheek cells placed on 'reflective' substrates that were aluminum-coated, compared to the conventional transparent substrates.[27] Subsequently, Lewis *et al*. reported the utility of another reflective substrate – stainless steel – for Raman spectroscopy, where a 43 – 64% increase in Raman signal was observed with stainless steel substrates compared to the traditional CaF_2 substrates.[28] With minimal Raman background and excellent biocompatibility, stainless steel is also durable and inexpensive to manufacture on a large scale for routine clinical/translational research.

Despite the aforementioned advantages, there are very limited studies that have fully explored the potential of stainless steel for characterizing cancer cells using Raman spectroscopy in translational/clinical research. For this study, we therefore first sought to evaluate the Raman signal intensity and quality for an extended range of BC cell-lines (TNBC/HER2- and HER2+ phenotypes), which were seeded on stainless steel and CaF_2 substrates. In an additional subset of experiments, we also attempted to compare the enhancement of Raman signal intensity of stainless steel with another viable Raman substrate – aluminum, with CaF_2 substrate serving as baseline. Subsequently, we assessed the discriminant ability of Raman signals generated from stainless steel and CaF_2 substrates to successfully characterize BC cells based on (i) cell-line type and (ii) HER2 status. In addition, we interrogated the influence of select experimental variables – excitation wavelength, laser power, exposure time, and cell-fixation – that may affect the quality of the Raman signal generated from both substrates. Lastly, we quantitatively analyzed

the Raman spectral traits of the selected BC cell-lines in a ratio-metric manner to understand the inherent biochemical differences between TNBC/HER2- and HER2+ phenotypes of BC, with additional validation using Coherent Anti-Stokes Raman Scattering (CARS) microscopy. The eventual goal of this study is to further explore the feasibility of stainless-steel as a reliable Raman substrate to successfully characterize and differentiate various biochemical traits for aggressive BC phenotypes, which can ultimately be vital in understanding BC pathogenesis and overcoming therapy-resistant BC.

Material & Methods

Cell Culture:

MDA-MB-231 (TNBC, HER2-, Claudin-low), MDA-MB-468 (TNBC, HER2-, Basal-type), AU565 (HER2+) and SKBr3 (HER2+) cells were obtained from the American Type Culture Collection (ATCC, Virginia, USA) and grown in Dulbecco's Modified Eagle Medium (Gibco – Thermo Fischer Scientific, Massachusetts, USA), which was supplemented with 10% fetal bovine serum (Gibco – Thermo Fischer Scientific, Massachusetts, USA) and 5% penicillin-streptomycin antibiotic mixture (Gibco – Thermo Fischer Scientific, Massachusetts, USA). The BC cells were maintained at 37^0C and 5% CO_2 concentration in a cell culture incubator.

Sample preparation:

For comparing substrates, 20mm × 1mm Raman-grade CaF_2 discs (Crystran, Poole, UK) and polished stainless-steel (316 Stainless steel, McMaster-Carr, Georgia, USA) discs of similar dimensions were considered (**Figure 1**). The substrates were first sonicated in 70% ethanol (Thermo Fischer Scientific, Massachusetts, USA) for 15 minutes and subsequently rinsed with sterile phosphate-buffered saline and air dried in a cell culture (laminar flow) hood. The aforementioned BC cells were then seeded in a sterile manner onto the corresponding substrates and allowed to incubate for approximately 48 hours in the cell culture incubator to reach

confluence. Following incubation, the cell culture medium was removed and the substrates were washed thrice with phosphate-buffered saline. Since the working distance of the objective in the described system permits only a thin film of water to keep cells/samples wet in its native form, it was not feasible to keep cells consistently wet over time. More importantly, gradual evaporation of this water film during successive Raman measurements could affect the background signal intensity significantly over time. To minimize background intensity variability from water loss/evaporation and consistency in signal quality, all the samples were air dried completely before spectral acquisition.

To study the influence of cell-fixation on Raman signal intensity, a set number of batches on CaF_2 substrate (**Table 1**) across all four cell-lines were fixed using 4% paraformaldehyde (Thermo Fischer Scientific, Massachusetts, USA) in phosphate-buffered saline for 10 minutes at room temperature (~22^0C) as previously described.[31] All batches on the stainless-steel substrates remained unfixed to minimize paraformaldehyde-steel interactions. While stainless steel is typically inert, this strategy was considered to eliminate the potential of paraformaldehyde getting oxidized in the presence of metal/iron oxide layer that would have formed over stainless steel over time.[32] The reaction may potentially generate residual or intermediate formic acid complexes[33-35], which could lead to an additional variable that may affect cellular biochemistry and the resultant Raman spectra.

For solely comparing Raman signal intensity levels of stainless steel with that of aluminum, the technique described above was repeated where MDA-MB-468 cells (TNBC, HER2-, Basal-type) were seeded at similar density onto polished stainless-steel discs (316 Stainless steel, McMaster-Carr, Georgia, USA) and standard household aluminum foil (0.016 mm thickness, Total Home Aluminum Foil, Rhode Island, USA) of similar dimensions. Cells were additionally seeded on 20mm × 1mm Raman-grade CaF_2 discs (Crystran, Poole, UK), with CaF_2 substrate serving as the baseline reference for comparing Raman signal intensity variation measured from stainless

steel and aluminum.

Raman microspectroscopy:

The Raman system (Renishaw InVia Raman microscope, Gloucestershire, UK) utilized in this study has been pre-calibrated using neon lines during its primary installation. The system utilized neon calibration lines to calibrate the wavenumber axis of the instrument.[36, 37] The specific neon peaks used were determined by the laser wavelength (785 nm and 830 nm) and the corresponding grating. These neon spectra had been collected and evaluated for proper focusing during the system installation. Since the system has always been stationed steadily with no changes in position of spectrometer components or ambient lab environment, it can be assumed that no significant change/deviation has occurred in the spectral axis. In addition, the system was always calibrated to the 520.5 cm^{-1} line of an internal silicon reference as a daily calibration check to ensure that the calibrated wavenumber axis is still aligned and correct for any small drift.

Spectral acquisition:

Raman spectrum were always obtained using a 50 × 0.75 NA objective (Leica Microsystems Inc., Buffalo Grove, Illinois). Per each 50X field, a single breast cancer cell was randomly selected and Raman spectra were obtained on at least 3 sites of the cell (East Zone, Center Zone and West Zone of the cell). For each experimental batch, this methodology was repeated over at least 5 and up to 20 breast cancer cells randomly selected over different 50X fields. The experimental measurements were repeated in at least 2 batches and up to 5 batches for validation of spectral findings. Raman spectra were acquired under parameters described in **Figure 1** and **Table 1**, with either a 785 nm diode laser (Innovative Photonic Solutions, Monmouth Junction, New Jersey) or an 830 nm diode laser (modular to the Renishaw InVia system).

Spectral processing:

After spectral acquisition, cosmic ray removal was first performed using Renishaw WiRE 4.2

software. All spectra were then baseline corrected to remove background fluorescence using the asymmetric least squares method as written in MATLAB R2020b software (Mathworks. Inc., Natick, MA, USA).[38] The baseline-corrected spectra was sequentially smoothed for noise using a second-order Savitzky-Golay filter. To account for inherent variation in intra- and inter-sample absolute signal intensities, the spectra were normalized to their respective mean intensity in the fingerprint (FP) range of 700 to 1780 cm^{-1} and high wavenumber (HW) range of 2600 to 3360 cm^{-1}. For spectra obtained with 830 nm excitation, Raman spectra were not acquired in the HW range as the system was not sensitive enough to detect Raman shifts beyond 2525 cm^{-1} (corresponds to 1050 nm) at this particular excitation wavelength.

Determination of Signal-to-Noise Ratio on non-normalized Raman spectra for different substrates:

The signal-to-noise ratio (SNR) of Raman measurements was estimated by acquiring five spectra from each of the four BC cell lines at powers ranging from 0.055 – 5.5 mW and exposure times varied from 3 – 15 sec for the two substrates (stainless steel and CaF_2). It must be noted that SNR determination was performed on each fluorescence-subtracted non-normalized spectrum obtained from BC cell lines, which was calculated using the following equation, as described earlier[39]:

$$SNR = \frac{S}{\sigma}$$

Here, S stands for the Raman peak height at 1450 cm^{-1} for FP spectra and 2925 cm^{-1} for HW spectra. σ denotes the spectral noise, which was defined as the standard deviation of Raman-silent regions between 1750-1780 cm^{-1} and 3100-3340 cm^{-1} for FP and HW spectra, respectively. The values reported in **Table 2** represent the average of SNR values that were calculated on a per-spectrum basis for five spectral measurements for each radiant exposure condition.

For each of the four BC cell-lines studied, the SNR values from stainless steel substrate were then compared to SNR measured from CaF_2 substrate to determine the Raman signal intensity

variation. The increase in signal afforded by stainless steel substrate, taken as the ratio between SNR from each substrate, is denoted by the 'SNR Amplification Factor' in FP and HW wavenumber regions. Subsequently in a separate experimental setup using only MDA-MB-468 cell lines, SNR values and SNR Amplification Factors was similarly determined and compared accordingly for stainless steel and aluminum foil, with respect to CaF_2 substrates.

After preliminary SNR comparison between stainless steel and CaF_2 substrates, Raman acquisition parameters were then optimized to yield comparable Raman signal intensity (absolute counts) for (i) the different substrates and (ii) Raman excitation wavelengths, for subsequent BC cell-line spectral characterization intended for the study design. The final Raman acquisition parameters for the BC cell lines, the number of cells assessed, and the corresponding number of spectra for each group are listed in **Table 1.**

Discrimination algorithm development and spectral classification accuracy determination.

Post-processed, mean normalized Raman spectra were used as inputs to train a multivariate Linear Discriminant Analysis (LDA) model to classify spectra based on (i) BC phenotype (cell-line) and (ii) HER2 status. LDA is a supervised analytical method for classifying Raman spectra, which determines the optimal data projection directions that maximize differences between samples from different groups and minimize differences between samples within the same group.[40, 41] Prior to LDA training, the spectral data set was first transformed using Principle Component Analysis (PCA) for initial dimensionality reduction to avoid overfitting and improve the robustness of the model. The first 15 PC scores accounted for ~95% of explained variance and were used as input variables to generate a diagnostic LDA classifier. To verify the performance and generalizability of this discriminant model based on PCA-LDA, cross-validation was performed using a leave-one-cell-out scheme to minimize bias. The leave-one-cell-out scheme involves leaving out all spectra measured from a single cell for testing, while the remaining dataset was used for model training. PCA-LDA statistical analyses were performed using MATLAB

software (Mathworks 2020b. Inc., Natick, MA, USA).

Evaluation of Raman spectra, ratio-metric assessment and statistical analysis:

Post-processed, mean normalized Raman spectra for BC cell-lines were assessed for spectral changes based on (i) HER2 expression status, (ii) underlying substrate – stainless steel versus CaF_2, (iii) excitation laser wavelength utilized – 785 nm versus 830 nm and (iv) influence of 4% paraformaldehyde fixation – fixed versus unfixed cells. Specific Raman spectral ratios indicative of relevant biochemical traits – lipid content, degree of lipid unsaturation, extent of lipid esterification/peroxidation, carbohydrate content and nucleic acid content – were calculated and compared across (i) BC cell phenotypes and (ii) HER2 status. A one-way analysis of variance (ANOVA) followed by a multiple comparison test using Tukey's honest significance was performed to test whether the selected Raman peak ratios between each cell type (phenotype) and HER2 status were significantly different (0.05*, 0.01**, 0.001***).

CARS imaging and analysis:

Correlation with the RS findings obtained from the assessed BC cell lines was achieved by conducting CARS imaging on the corresponding cells to visualize the spatial distribution of lipids. CARS imaging was performed using a custom-built multimodal imaging platform that was designed and calibrated as described earlier.[42] Cells were seeded on uncoated glass bottom petri dishes (1.5 Coverslip, 35 mm diameter, Mattek, USA) 48 hours before CARS imaging. The cells were subsequently imaged on the epi-detection port, which is equipped with a photomultiplier tube (GaAsP Amplified PMT, Thorlabs, USA). CARS imaging at 2850 cm^{-1} was conducted using pump and Stokes wavelengths of 798 and 1040 nm, respectively. Each CARS image was acquired for 10 microseconds/pixel using a 20x water immersion objective (Olympus XLUMPLFLN, 1.0NA) with a high spatial sampling density (206 nm/pixel) covering 512 x 512 pixels per image (Field of View for each image: 105 μm × 105 μm). To compare lipid droplet content within each cell line, CARS images were processed to quantify the percentage of cell

area occupied by lipid droplets on a per-cell basis. **Figure 2** outlines the image processing steps used, where images were first background subtracted to remove baseline intensity variation. A thresholding level was then set manually to create a binary image that best represented image regions which contained lipid droplets. A binary filter was then applied to eliminate random noise from pixels with intensity values near the threshold, but not associated with droplets. Finally, regions of interest (ROIs) were drawn manually around each cell so that the percent area could be calculated by the ratio of bright pixels (i.e., lipid droplets) to total pixels within each cell's ROI. Image analysis and segmentation were performed in ImageJ (U.S. National Institute of Health).

Results

Comparing SNR of non-normalized Raman spectra for BC cell lines on stainless steel versus CaF_2 substrates

A substantial increase of Raman signal intensity was observed at 1003 cm^{-1} and 1450 cm^{-1} for FP spectra (**Figure 3**) and 2850 cm^{-1} and 2925 cm^{-1} for HW spectra (**Figure** 4) in all four cell-lines on stainless steel relative to CaF_2 substrate. As demonstrated in **Table 2**, the SNR of Raman spectra was notably increased across all four BC cell-lines on stainless steel compared to CaF_2 substrate. Upon calculating the amplification factor, SNR was found to be more amplified for the TNBC/HER2- cell-lines (MDA-MB-231 and MDA-MB-468) with an increase ranging from 50 – 250% in FP spectra and 50 – 200% in HW spectra. The Raman SNR amplification for stainless steel was comparatively lower for HER2+ cell-lines (SKBr3 and AU565) with an increase of 40 – 140% in FP spectra and 10 – 180% in HW spectra. Similarly, the rise in Raman signal intensity of stainless steel relative to CaF_2 substrate with increasing incident laser energy on substrate (0.165 mJ – 82.5 mJ) was lower for HER2+ cell-lines, as compared to TNBC/HER2- cell-lines. The findings were observed to be consistent at 1003 cm^{-1} and 1450 cm^{-1} for FP (**Figure 3**) as well as at 2850 cm^{-1} and 2925 cm^{-1} for HW spectra (**Figure 4**). In addition, the most pronounced increase of SNR amplification factor for Raman signal from BC cell-lines on stainless steel

compared to CaF_2 substrate was noticed at an incident laser energy of 1.65 mJ (incident laser power on sample = 0.55 mW). Overall, AU565 yielded strongest Raman signal intensity for both substrates with varying laser powers. However, it also demonstrated the lowest SNR amplification factor on stainless steel relative to CaF_2 substrate.

Raman signal intensity comparison between stainless steel, aluminum and CaF_2 substrates.

Analysis of Raman spectra from all 3 substrates indicated that aluminum provided stronger Raman signal counts over stainless steel and CaF_2 substrates in both the fingerprint and the high wavenumber regions (see **Supplementary Figure 1**). However, aluminum also exhibited higher background noise intensity in the finger print region. Compared to steel, the aluminum substrate spectral background increased by roughly ~130% (**Supplementary Figure 1A**), while the Raman component increased by only 30% (**Supplementary Figure 1C**). As a result, stainless steel yielded a better net signal-to noise (SNR) ratio than aluminum in the FP region, with stainless steel having an average SNR amplification factor of 2.39 versus aluminum at 2.15 (**Supplementary Table 1**). In contrast, the background noise for aluminum was notably lower in the HW region than the FP region, while maintaining amplification of the Raman signal. This led to aluminum yielding an improved net signal-to noise (SNR) ratio than stainless steel in the HW region, with aluminum having an average SNR amplification factor of 3.33 versus stainless steel at 2.3. Another observation from these measurements is that raw spectral counts between measurements varied more on the aluminum foil substrate, leading to higher deviations across measurement positions with aluminum compared to steel for both the FP and HW regions (**Supplementary Figure 1A** and **1B**).

Classification accuracy of Raman spectra for BC cell lines on stainless steel versus CaF_2 substrates

LDA of FP Raman spectra obtained from unfixed BC cells on stainless steel yielded a superior 96% accuracy in BC cell type discrimination, compared to that from CaF_2 substrate that provided

89.8% accuracy (**Figure 5** and **6**). Classification accuracy for FP spectra on stainless steel substrate remained comparable for different excitation laser wavelengths at accuracies of 96% for 785 nm and 98.6% for 830 nm. Accuracy in BC cell type classification was noted to be the lowest at 74.8% for FP Raman spectra obtained from fixed BC cells grown on CaF_2 substrate. LDA classification accuracy was inferior for HW Raman spectra at 66% for unfixed cells on stainless steel plates, while unfixed and fixed cells on CaF_2 substrates yielded accuracies of 66.7% and 51% respectively.

When LDA was applied for discriminating BC cell-lines based on HER2 status, it is important to note that the number of linear discriminate dimensions useful in describing variances between the classes is limited to the number of discriminant groups minus one.[43] So, for discrimination between 2 groups, i.e., HER2+ versus HER2-, only a single linear discriminant dimension is used to visualize separation of HER2 status, as seen in **Figure 7**. FP spectra from unfixed cells on stainless steel and CaF_2 were both classified with an accuracy of 100% on the basis of HER2 status, while FP spectra from fixed BC cells seeded on CaF_2 substrates provided a comparable accuracy of 95% (**Figures 7** and **8**). In parallel, excitation wavelength had negligible influence on HER2 status classification for FP spectra from stainless steel with 100% accuracy at 785 nm and 99.2% accuracy at 830 nm. As observed for BC cell type discriminant analysis, classification accuracy for HER2 status was also remarkably lower for HW spectra with 83.7 % accuracy from unfixed cells on stainless steel plates, while unfixed and fixed cells on CaF_2 substrate yielded 85.8% and 75.3% accuracy respectively.

Spectral analysis and characterization of BC cell lines based on HER2 expression status

Averaged mean normalized Raman spectra demonstrated prominent spectral differences in FP and HW regions between TNBC/HER2- cells (MDA-MB-231 and MDA-MB-468) and HER2+ cells (AU565 and SKBr3) as indicated by the shaded areas in **Figures 9** and **10**. Based on the Raman spectral assignments described in **Table 3**, the most notable spectral differences appear in the

region associated with lipid bands. In the FP region, spectra from HER2+ cells demonstrated increased intensity at 1068-1082 cm^{-1} (C-C stretch of acyl chain in lipids), 1301 cm^{-1} (CH_2 twist/wag in lipids) and 1440 cm^{-1} (CH_2 bending in lipids). In the HW region, there was a marked rise in the intensity at 2850 cm^{-1} (CH_2 symmetric stretch in lipids). On the other hand, a distinct feature for TNBC/HER2- cells was the increase in intensity at 1656 cm^{-1} (C=C stretch in lipids) which typically serves as a spectral marker for the degree of lipid unsaturation. Furthermore, FP spectra from TNBC/HER2- cells uniquely exhibited an increase in intensity at 782 cm^{-1}, which is a prominent Raman band representing nucleic acids. More importantly, these spectral differences between HER2+ and HER2- cells were consistently observed with (i) different substrates – stainless steel versus CaF_2 substrate (**Figure 9**), (ii) different excitation wavelengths – 785 nm versus 830 nm – on stainless steel substrate (**Figure 10**) and (iii) unfixed versus fixed BC cells (**Figure 9**). PCA of the Raman spectra further highlights these spectral differences reliably between HER2+ and HER2- cells, with the aforementioned lipid bands being attributed to PC1 that was responsible for up to 62.5% and 82.7% of explained variance in FP and HW regions respectively (**Supplementary Figure 2** and **3**).

Based on the assignments in **Table 3**, Raman peak ratio calculations were used to ascertain relative spectral changes between HER2+ and TNBC/HER2- cells grown on stainless steel. In agreement with the findings described above, the 1301/1255 cm^{-1}, 1440/1255 cm^{-1} and 2850/2925 cm^{-1} peak ratios were markedly elevated for HER2+ cells ($p<0.001$), denoting a significant increase in lipid content relative to proteins (**Figures 11A – 11C**). In contrast, the 1656/1440 cm^{-1} ratio was more elevated for TNBC/HER2- cells ($p<0.001$), signifying a higher amount of unsaturated lipids relative to total lipids in these cells (**Figure 11D**). **Figure 12A** illustrates that the 1741/1656 cm^{-1} ratio is significantly higher in HER2+ cells ($p<0.001$), possibly representing elevated lipid esterification/peroxidation. Meanwhile, the 940/830 cm^{-1} ratio was found to be higher in TNBC/HER2- cells (**Figure 12B**), indicating an increase in carbohydrates relative to amino acids in these cells ($p<0.001$). Lastly, the 782/830 cm^{-1} ratio representing nucleic

acid content was increased for HER2- cells (**Figure 12C**), attaining significance particularly for MDA-MB-468, a basal-subtype of TNBC cell-lines ($p<0.001$). While similar ratiometric trends were observed for Raman peak ratio calculations measured from HER2+ and TNBC/HER2- cells grown on CaF_2 substrates (**Supplementary Figure 4** and **5**), the observed boxplot data variance bars were larger for the CaF_2 dataset compared to that of stainless steel.

CARS findings for BC cell lines based on HER2 expression status

Upon imaging TNBC/HER2- (MDA-MB-231 and MDA-MB-468) and HER2+ (AU565 and SKBr3) cells with CARS microscopy conducted at 2850 cm^{-1} resonance, subcellular structures as lipid droplets were clearly visualized, due to the CH_2 symmetric stretch mode from lipids. The images revealed a higher number of lipid droplets in HER2+ cells compared to TNBC/HER2- cells (**Figure 13A – 13D**). Upon quantifying the percentage of cell area covered by lipid droplets (as described earlier in **Figure 2**), it was found that lipid droplets occupied about 2.5 – 4 times greater percentage of area in HER2+ cells compared to TNBC/HER2- cells ($p<0.001$) (**Figure 13E**). These findings observed with CARS microscopy further denote elevated lipid content in HER2+ cells, corroborating and providing spatial context to the point-based spectra obtained from BC cells grown on stainless steel and CaF_2 substrates scanned with microspectroscopy (**Figures 9** and **10**).

Discussion

Raman spectroscopy has lately emerged as a promising modality that can aid in non-invasively exploring the molecular basis of BC. In addition, Raman spectroscopy could yield quantifiable biochemical information that can be invaluable for comprehending aggressive phenotypes of BC or identifying prospective therapeutic targets. While pursuing these overarching endpoints to predict patient prognosis and optimize BC therapy with Raman spectroscopy, one must also recognize the innate weak nature of Raman signals from biological specimens. Longer measurement times or use of higher laser power on samples might be necessary to obtain optimal

Raman signals, which may simultaneously impede widespread adoption of Raman spectroscopy for routine clinical/translational research. Therefore, it becomes imperative to explore simple and low-cost means to enhance Raman signals from biological samples. In this study, we sought to demonstrate how stainless steel could be a cost-effective Raman substrate for delivering improved Raman SNR with reduced scan times and lower laser power. Prior studies that have investigated the potential of stainless steel as a Raman substrate have either purely examined its ability to improve Raman signals in cells[28] or have solely explored its potential for cancer diagnostics (to distinguish cancerous versus healthy samples).[44] Our study has gone further to explore the utility of stainless steel for BC prognosis assessment and scope for therapy guidance. The ability of stainless steel to boost Raman signal and provide ample biochemical information to discriminate BC phenotypes was uniquely explored in this study. The enhanced spectral information obtained with this approach is immensely valuable for effectively assessing breast cancer prognosis, identifying traits of tumor aggressiveness or guiding tailored/targeted therapy, e.g., discriminating HER2+ versus HER2- type BC. The study further compared Raman signal enhancement with stainless steel substrate in both the fingerprint region as well as the high wavenumber region.

A variety of substrates including aluminum coated glass, thin-film gold coated substrate, borosilicate glass, synthetic fused silica, extra white soda lime glass and others, have been previously investigated to overcome the limitations of weak Raman SNR and high costs associated with the traditional CaF_2 substrate.[27, 28, 45] Stainless steel has the notable advantages of being easily accessible, robust/durable, relatively cheap and highly biocompatible. In our study, BC cells were found to easily attach, multiply and retain expected morphology with equal propensity on stainless steel compared to CaF_2 substrate (**Figure 1**), which had also been observed with U-2 OS (human bone osteosarcoma) cells by Lewis *et al.*[28] The caveat to the aforementioned findings being that only cancer cell-lines were utilized for comparing Raman SNR on these substrates, with the implications for non-cancerous primary cells currently remaining

unknown. While primary cells such as fibroblasts and osteoblasts have been successfully cultured on stainless steel[46-48], further investigations are needed to compare morphology and behavior of primary cells on stainless steel versus CaF_2 substrates, since primary cells require more stringent culturing conditions.

Lewis *et al.* reported a median improvement of Raman SNR in cells at 1450 cm^{-1} by a factor of 2.32 (increase of 132%)[28]. In this study, we also observed an increase of Raman SNR by a factor of 2.19 (increase of 119%) at 1450 cm^{-1} on stainless steel as compared to CaF_2 substrate when averaged across all radiant exposure levels. In addition, we also noted the averaged increase of Raman SNR in the HW range at 2925 cm^{-1}, amplified by a factor of 2.22 (increase of 122%). The observed increase of Raman SNR on reflective substrates, such as stainless steel, could be explained by laser photons incident on a reflective surface being redirected back through the sample (cells/tissue) where these photons can then get Raman scattered in the a 'second-pass', resulting in a definite increase in Raman scattering intensity from the sample that improves the detected signal intensity.[28, 49, 50] The observed difference and variability in SNR increase at 1450 cm^{-1} between both studies can however be attributed to the fact that SNR comparison in the earlier study was performed only on one cell type (bone osteosarcoma) and at a single laser power/energy fluence.[28] For the substrate comparison in our study, SNR amplification had been averaged from four distinct BC cell types and varying laser power/energy fluences (**Table 2**). Another potential contributing factor could be the differences in the surface quality/polishing of the stainless steel substrates used by each group. A key finding in our study was the stronger Raman signal from HER2+ cells on both substrates, which can be attributed to the relatively higher lipid content in these cells.[22, 23] Lipids with their longer non-polar acyl chains possess (i) a higher Raman cross-section (three times higher than proteins at 1440 cm^{-1}) and (ii) greater optical scattering in biological tissues[51-54], leading to more robust Raman signals from lipid-rich samples, as evidenced with HER2+ cells in this study (**Table 2**, **Figure 3** and **Figure 4**). With a comparatively weaker SNR on CaF_2 substrate, TNBC/HER2- cells experienced a considerable

boost in Raman signal intensity on stainless steel (up to 250% in FP and 200% in HW spectra). The Raman SNR amplification on stainless steel for HER2+ cells was relatively lower (up to 140% in FP and 180% in HW spectra) since these cells already had stronger Raman signal intensity on CaF_2 substrate itself as described earlier.

Our study was able to further compare the signal enhancement of stainless steel with that of another viable Raman substrate – aluminum for the first time. Earlier studies have already demonstrated the immense potential of aluminum as a prospective Raman substrate, due to aluminum's distinct property as a plasmonic material.[27, 55] Our data analysis indicated that aluminum overall indeed provided stronger Raman signal counts over stainless steel and CaF_2 substrates in both the FP and the HW regions (**Supplementary Figure 1**). However, with regards to SNR determination, aluminum scored lower than stainless steel in the FP region, mainly because the higher background in aluminum substrate in FP region would typically not provide usable signal, but possibly induced more shot noise onto the Raman spectrum leading to a lower SNR. In contrast, Raman SNR with aluminum was superior to that of stainless steel and CaF_2 substrates in the HW range, as the background was comparably lower for aluminum in the HW range. It must be further noted that multiple factors could influence the SNR levels determined on these substrates – surface roughness/polish in substrate (degree of substrate reflectivity), excitation wavelength (longer wavelength have lower background fluorescence in the fingerprint region), or cell type/degree of cell confluence on substrate. More detailed studies are warranted ahead to assess the influence of these parameters while comparing Raman signal between biocompatible substrates such as stainless steel and aluminum. Nonetheless, our findings imply that both stainless steel and aluminum are biocompatible and cost-effective materials that could serve as viable Raman substrates, each of them with their own distinct advantages.

Due to enhanced SNR on stainless steel substrate, LDA of Raman spectra obtained from stainless steel generated superior or comparable classification accuracy for BC cells compared to that from CaF_2 substrate (**Figure 5 – 8**), while employing only 18 – 22% of incident laser power

and 50 – 66% of exposure time required for CaF_2 substrate as described in **Table 1**. While no substantial difference was observed in classification accuracy or spectral quality on stainless steel for 785 nm vs 830 nm excitation source, it must be noted that stronger Raman signal from biological specimens at 785 nm[27] resulted in decreased acquisition times compared to the 830 nm (**Table 1**). Excitation at 830 nm, however, would provide a SNR benefit for highly fluorescent samples since the degree of background fluorescence signal could be mitigated by longer laser wavelengths. A pertinent aspect of our findings includes how the fixation of cells on CaF_2 substrates considerably reduced spectral classification accuracy compared to the unfixed cells on either substrate. It is likely that even the mildest fixative (as used in this study) could still cause definitive changes in lipids and protein conformations in cells[31], possibly leading to alterations/loss of spectral traits relevant for classification, compared to unfixed cells.

Spectral analyses further revealed notable differences between BC cell types based on phenotype/HER2+ expression status (**Figures 9** and **10**). The most striking spectral feature was the consistent elevation of lipid-dominant peaks in HER2+ cells, indicative of increased lipid content in these cells. These spectral features where also validated by the increased lipid droplet content of HER2+ versus TNBC/HER2- cell lines seen in the CARS images (**Figure 13**) that was able to uniquely provide a spatial context to lipid-related spectral changes observed in our study measured with the conventional point Raman measurements. Increased lipogenesis in HER2+ cells has been previously reported and has been attributed to overexpression of the 'fatty acid synthase' enzyme.[56-58] Fatty acid synthase augments fatty acid synthesis which endows survival benefits to HER2+ cells, rendering them highly aggressive. In turn, fatty acid synthase was found to be expressed at a relatively lower level in TNBC/HER2- cells as compared to HER2+ cells[57], in agreement with the ratio-metric analysis and CARS findings of our study (**Figure 11A – 11C** and **Figure 13**). An elevated 1656/1440 cm^{-1} ratio for TNBC/HER2- cells (**Figure 11D**), suggestive of a relative increase in unsaturated fatty acids, was also previously reported.[23, 59] A likely explanation for this observation could be increased expression of the cyclooxygenase-2 enzyme

in TNBC/HER2- cells[60-63], resulting in increased prostaglandins that are mainly composed of unsaturated fatty acids. In contrast, HER2+ cells yielded an increased 1741/1656 cm^{-1} ratio (**Figure 12A**) indicative of higher lipid peroxidation, possibly due to higher oxidative stress and increased reactive oxygen species production within HER2+ cells.[59, 64] Furthermore, the state of elevated lipogenesis and oxidative stress alongside heightened glycolysis in HER2+ cells[65] could lead to rapid breakdown/conversion of carbohydrates into lipids. At the same time, increased expression of glucose transporter-1 protein may cause higher glucose uptake or influx into TNBC/HER2- cells.[66, 67] The combinatorial effect of these two events might explain the increased 940/830 cm^{-1} ratio for TNBC/HER2- cells over HER2+ cells (**Figure 12B**). Compared to other BC cells, MDA-MB-468 (TNBC basal subtype) demonstrated the highest value for the 782/830 cm^{-1} ratio which may spectrally correlate with increased nucleic acid content (**Figure 12C**). Our findings concur with earlier reports which also indicated that the TNBC basal subtype had the highest proliferative index among the various BC subtypes, along with a high mitotic count.[68] The ratiometric trends were similarly reflected from the spectral data between HER2+ and TNBC/HER2- cells grown on CaF_2 substrates as well (**Supplementary Figure 4** and **5**). However, the boxplot variance bars were observed to be higher in the CaF_2 dataset, as when compared to that of stainless steel. These findings further underscore on the improved SNR that yields superior discriminant capability as observed with stainless steel (**Figure 5** and **6**). Still, Raman ratios from both stainless steel and CaF_2 substrate were consistent in indicating (i) higher level of lipid content in HER2+ cells and (ii) higher degree of lipid unsaturation in TNBC/HER2- cells.

It must be further reiterated that these subtle, yet distinctive spectral changes between different BC cell types were successfully highlighted in our study due to improved Raman signal from stainless steel at lower acquisition times and reduced laser powers. These two advantages would allow quicker scan times for biological specimens/samples, while ensuring minimal tissue degradation. Improved SNR can also be leveraged during Raman mapping of tissues performed on stainless steel substrate, as demonstrated by Lewis *et al.*[28] This further opens up the

opportunity of providing a pathologist with biochemical details of tissues/biological specimens via information-rich hyperspectral Raman maps within a clinically feasible duration time. Moreover, stainless steel is easily accessible, durable and extremely cost-effective, making it a viable substrate onto which tissue sections/biological specimens can be overlaid and effortlessly implemented into routine clinical work-flow. In addition to tissue/cellular morphology seen with conventional histology, Raman maps of tissue sections obtained on stainless steel could allow for a greater number of spectral features to be visualized. This may potentially provide further insights into tissue sections at a biochemical level. Furthermore, these spectral signatures can allow enhanced characterization of biochemical traits related to tumor aggressiveness, metastatic tendencies or drug resistance, which can be highly effective for improving BC management. However, it should be noted that the SNR amplification provided by stainless steel substrate might be relatively lower when scanning tissue sections, that tends to be thicker and less transparent than confluent cell layers. Lewis *et al*. had similarly observed an average Raman signal increase of 1.43 times during analysis of tissue sections versus 1.64 times when analyzing cells.[28] The degree of SNR amplification might therefore be dependent on the thickness and opacity of tissue section because less laser radiation would be able to reflect off the substrate for second-pass through a thicker tissue section/sample.

Conclusion

Our study successfully demonstrated a significant enhancement of Raman signals on stainless steel substrate for both FP and HW spectra across all BC cell types employed in this study, while utilizing only a fraction of the acquisition time and laser power that are routinely used for CaF_2 substrates. Improved Raman SNR on stainless steel led to enhanced spectral characterization of BC cells, yielding superior or comparable classification accuracies based on phenotype or HER2 expression status, when compared to CaF_2 substrate. Further data analysis unveiled various spectral differences between HER2+ and TNBC/HER2- cells, with the most prominent trait being

the presence of significantly increased lipid content in HER2+ cells that was further correlated with CARS imaging. Our results concur with earlier findings that suggested stainless steel could be a low-cost and durable Raman substrate alternative. Improved SNR with stainless steel at quicker acquisition times and reduced laser power can enable optimized biochemical analysis using detailed Raman signatures. Rapid scan times of biological specimens/tissues with stainless steel could enable successful translation of Raman micro-spectroscopy for use within routine clinical workflow, which can further facilitate our understanding of BC pathogenesis and provide insights to optimize BC therapeutics.

Author Contributions

G.T, S. F, R. G, F.C, E. H, P. R, W. R. A and A.M-J were involved in preparing the manuscript. G.T., S. F, R. G. and F.C. were responsible for spectral acquisition studies. G. T, S. F, R. G and E.H conducted analysis of the spectral data acquired. G. T, S. F, F. C and P. R was responsible for cell culture and seeding cells on different substrates. G. T, R. G and S.F performed CARS imaging studies described in the study.

Acknowledgements

The authors acknowledge the financial support of the Breast Cancer Research Program Idea Expansion Award #W81XWH-14-1-0278 from the Department of Defense (to A.M-J). We are thankful to Isaac Pence for his insight that aided the study design described in the manuscript.

Data Availability

The data generated during this study are included in this paper along with supplementary data files. The complete dataset is available from the corresponding author upon reasonable request.

Table 1: Experimental parameters used to characterize various breast cancer (BC) cell lines in study design. Parameters were first optimized to yield comparable Raman signal intensity (absolute counts) for different substrates and wavelengths, before being utilized for cancer cell characterization.

BC Cell lines	MDA-MB-231	MDA-MB-468	AU565	SKBr3	Total spectra: HER2-	Total spectra: HER2+	Total spectra analyzed	Cell Fixation	Measurement parameters for Raman microspectroscopy
Phenotype	Triple negative; Claudin-low	Triple negative; Basal	HER2 overexpressing						
HER2 status	HER 2-	HER 2-	HER 2+	HER 2+					
Substrate	Fingerprint wavenumber region (700 – 1750 cm^{-1})								
Stainless Steel	120 spectra 40 cells 2 batches	120 spectra 40 cells 2 batches	120 spectra 40 cells 2 batches	120 spectra 40 cells 2 batches	240	240	480	Unfixed	50X objective; Excitation λ:785 nm Time: 15 s (5 s × 3 accumulations) Laser power on sample: ~5.5 mW
	128 spectra 43 cells 3 batches	129 spectra 43 cells 3 batches	129 spectra 43 cells 3 batches	129 spectra 43 cells 3 batches	257	258	515	Unfixed	50X objective; Excitation λ:830 nm Time: 20 s (5 s × 4 accumulations) Laser power on sample: ~4.5 mW
CaF_2 Substrate	60 spectra 20 cells 2 batches	45 spectra 15 cells 2 batches	60 spectra 20 cells 2 batches	60 spectra 20 cells 2 batches	105	120	225	Unfixed	50X objective; Excitation λ:785 nm Time: 30 s (10 s × 3 accumulations) Laser power on sample: ~25 mW
	100 spectra 20 cells 5 batches	100 spectra 20 cells 5 batches	100 spectra 20 cells 5 batches	100 spectra 20 cells 5 batches	200	200	400	Fixed	50X objective; Excitation λ:785 nm Time: 30 s (10 s × 3 accumulations) Laser power on sample: ~25 mW
Substrate	High wavenumber region (2700 – 3200 cm^{-1})								
Stainless Steel	120 spectra 40 cells 2 batches	120 spectra 40 cells 2 batches	119 spectra 40 cells 2 batches	120 spectra 40 cells 2 batches	240	239	479	Unfixed	50X objective; Excitation λ:785 nm Time: 15 s (5 s × 3 accumulations) Laser power on sample: ~5.5 mW
	System is not sensitive to Raman shifts in high wavenumber region at 830 nm.								
CaF_2 Substrate	60 spectra 20 cells 2 batches	45 spectra 15 cells 2 batches	60 spectra 20 cells 2 batches	60 spectra 20 cells 2 batches	105	120	225	Unfixed	50X objective; Excitation λ:785 nm Time: 30 s (10 s × 3 accumulations) Laser power on sample: ~25 mW
	100 spectra 20 cells 5 batches	100 spectra 20 cells 5 batches	100 spectra 20 cells 5 batches	100 spectra 20 cells 5 batches	200	200	400	Fixed	50X objective; Excitation λ:785 nm Time: 30 s (10 s × 3 accumulations) Laser power on sample: ~25 mW

Table 2: Signal-to-Noise Ratio (SNR) comparison for non-normalized Raman spectra from breast cancer (BC) cells at 1450 cm^{-1} (fingerprint region) and 2925 cm^{-1} (high wavenumber region) on stainless steel (SS) vs CaF_2 substrate.

Incident Energy	BC Cells	SNR at 1450 cm^{-1}				SNR at 2925 cm^{-1}			
		SS	**CaF_2**	**Stainless Steel SNR amplification factor**	**Signal change (in %)**	**SS**	**CaF_2**	**Stainless Steel SNR amplification factor**	**Signal change (in %)**
0.165 mJ Laser power on sample: **~0.055 mW** Time: **3 s** (1 s × 3 accumulations)	MDA-MB-231	3.3	2.2	1.5	+50%	3.9	2.4	1.6	+60%
	MDA-MB-468	4.9	2.8	1.8	+80%	3.6	2.4	1.5	+50%
	AU565	5.0	2.9	1.7	+70%	2.4	2.3	1.1	+10%
	SKBr3	4.5	2.2	2.0	+100%	3.7	2.3	1.6	+60%
1.65 mJ Laser power on sample: **~0.55 mW** Time: **3 s** (1 s × 3 accumulations)		**SS**	**CaF_2**			**SS**	**CaF_2**		
	MDA-MB-231	12.9	3.7	3.5	+250%	9.2	3.1	3.0	+200%
	MDA-MB-468	11.7	3.8	3.1	+210%	6.6	3.2	2.1	+110%
	AU565	13.7	5.7	2.4	+140%	6.0	3.0	2.0	+100%
	SKBr3	12.6	5.3	2.4	+140%	7.6	3.1	2.5	+150%
16.5 mJ Laser power on sample: **~5.5 mW** Time: **3 s** (1 s × 3 accumulations)		**SS**	**CaF_2**			**SS**	**CaF_2**		
	MDA-MB-231	32.1	10.9	2.9	+190%	29.5	11.1	2.7	+170%
	MDA-MB-468	31.0	9.8	3.2	+220%	22.6	10.2	2.2	+120%
	AU565	30.1	15.8	1.9	+90%	27.2	10.1	2.7	+170%
	SKBr3	31.5	18.0	1.8	+80%	27.9	10.0	2.8	+180%
82.5 mJ Laser power on sample: **~5.5 mW** Time: **15 s** (5 s × 3 accumulations)		**SS**	**CaF_2**			**SS**	**CaF_2**		
	MDA-MB-231	66.4	33.1	2.0	+100%	123.0	50.1	2.5	+150%
	MDA-MB-468	67.0	32.6	2.1	+110%	94.4	48.0	2.0	+100%
	AU565	64.6	47.2	1.4	+40%	127.4	51.9	2.5	+150%
	SKBr3	68.8	48.8	1.4	+40%	146.2	54.0	2.7	+170%

Table 3: Relevant wavenumbers observed in experimental data and the corresponding Raman spectral assignments. *(C=cytosine, T=thymine, A=adenine, G=guanine, U=uracil)

Wavenumber (cm^{-1})	Spectral assignments	References
719	C-N stretch lipids	69, 70
755 – 760	Symmetric ring breathing in tryptophan	69-71
782 – 788	782: Nucleic acid (C, T, U-ring breathing)*; 788: DNA backbone O-P-O stretching	69, 71, 72
810 – 811	RNA: backbone O-P-O stretching	69, 71, 73
830	Out-of-plane ring breathing tyrosine	69, 71
852	Ring breathing (tyrosine)	69
935 – 940	C-O-C stretching (glycogen, polysaccharides) and/or C-C stretch α-helix proteins	69, 71, 74
977	C-C stretching unordered/β-sheet (proteins)	69
1003	Symmetric ring breathing mode of phenylalanine	69
1031	C-H in plane bending of phenylalanine	69, 71
1068	C-C stretch acyl chains (trans) lipids	69
1082	C-O stretch, C-C stretch acyl chains (gauche) lipids	71
1090 – 1094	DNA backbone PO_2^- stretching	69, 71
1125	C-O stretch carbohydrates; C−C stretch acyl chains (trans) lipids	69
1204 – 1209	C-C_6H_5 stretch phenylalanine, tryptophan	71
1220 – 1310	Amide III: mostly NH in-plane bending and CN stretching	71
1301-1304	CH_2 twist/ wag/ deformation (lipids); amide III α-helical structures	69, 71
1338 – 1342	Nucleic acid (A, G)*; CH deformation carbohydrates	69, 71, 72
1440	CH_2 bending predominantly lipids	69, 71
1450	CH_2 bending predominantly proteins	69, 71
1576	Nucleic acid (A,G)*	69, 71, 72
1656	Predominantly C=C stretch lipids	69
1640 – 1680	Amide I: predominantly C=O stretch in proteins	71
1740 – 1741	C=O in lipids	69
2850	CH_2 symmetric stretch predominantly in lipids	69, 75
2883 – 2885	CH_2 asymmetric stretch, lipids and proteins	69, 75
2925 – 2930	CH_3 symmetric stretch predominantly in proteins and/or CH_2 asymmetric stretch	69
2970	CH_3 asymmetric stretch	69
3015	Alkyl ═C—H stretches	69

Supplementary Table 1: Signal-to-Noise Ratio (SNR) comparison for non-normalized Raman spectra from MDA-MB-468 (Triple Negative Breast Cancer (TNBC)/HER2- cells at 1450 cm^{-1} (fingerprint region) and 2925 cm^{-1} (high wavenumber region) on aluminum foil (AF) vs stainless steel (SS) vs CaF_2 substrate.

Incident Energy	**SNR at 1450 cm^{-1}**					**SNR at 2925 cm^{-1}**				
	AF	**SS**	**CaF_2**	**AF SNR amplification factor**	**SS SNR amplification factor**	**AF**	**SS**	**CaF_2**	**AF SNR amplification factor**	**SS SNR amplification factor**
0.165 mJ Laser power on sample: **~0.055 mW** Time: **3 s** (1 s × 3 accumulations)	3.5	3.3	2.0	1.8	1.65	3.3	3.3	2.0	1.7	1.7
1.65 mJ Laser power on sample: **~0.55 mW** Time: **3 s** (1 s × 3 accumulations)	8.8	9.0	3.0	2.9	3	8.1	5.8	3.4	2.4	1.7
16.5 mJ Laser power on sample: **~5.5 mW** Time: **3 s** (1 s × 3 accumulations)	22.5	28.1	10.4	2.2	2.7	27.5	15.2	5.8	4.7	2.6
82.5 mJ Laser power on sample: **~5.5 mW** Time: **15 s** (5 s × 3 accumulations)	52.6	66.5	30.8	1.7	2.2	84	60.1	18.5	4.5	3.2

References

1. Breast Cancer Facts and Statistics, https://www.breastcancer.org/facts-statistics, 2022).
2. R. L. Siegel, K. D. Miller, H. E. Fuchs and A. Jemal, *CA: A Cancer Journal for Clinicians*, 2022, **72**, 7-33.
3. M. J. Duffy, in *Advances in Clinical Chemistry*, ed. H. E. Spiegel, Elsevier, 1996, vol. 32, pp. 135-166.
4. I. Alroy and Y. Yarden, *Breast disease*, 1999, **11**, 31-48.
5. S. M. Ronen and M. O. Leach, *Breast Cancer Research*, 2000, **3**, 36.
6. A. M. Gonzalez-Angulo, F. Morales-Vasquez and G. N. Hortobagyi, in *Breast Cancer Chemosensitivity*, eds. D. Yu and M.-C. Hung, Springer New York, New York, NY, 2007, DOI: 10.1007/978-0-387-74039-3_1, pp. 1-22.
7. P. A. Corsetto, A. Cremona, G. Montorfano, I. E. Jovenitti, F. Orsini, P. Arosio and A. M. Rizzo, *Cell Biochemistry and Biophysics*, 2012, **64**, 45-59.
8. S. H. Jafari, Z. Saadatpour, A. Salmaninejad, F. Momeni, M. Mokhtari, J. S. Nahand, M. Rahmati, H. Mirzaei and M. Kianmehr, *Journal of Cellular Physiology*, 2018, **233**, 5200-5213.
9. S. Mukerjee, A. S. Saeedan, M. N. Ansari and M. Singh, *Membranes*, 2021, **11**, 479.
10. A. Mahadevan-Jansen and R. Richards-Kortum, *Journal of Biomedical Optics*, 1996, **1**.
11. G. Shetty, C. Kendall, N. Shepherd, N. Stone and H. Barr, *British Journal of Cancer*, 2006, **94**, 1460-1464.
12. H. Abramczyk and B. Brozek-Pluska, *Chemical Reviews*, 2013, **113**, 5766-5781.
13. I. R. M. Ramos, A. Malkin and F. M. Lyng, *BioMed Research International*, 2015, **2015**, 561242.
14. Q. Zheng, J. Li, L. Yang, B. Zheng, J. Wang, N. Lv, J. Luo, F. L. Martin, D. Liu and J. He, *Analyst*, 2020, **145**, 385-392.
15. H. Abramczyk, B. Brozek-Pluska, M. Kopec, J. Surmacki, M. Błaszczyk and M. Radek, *Cancers*, 2021, **13**, 960.
16. P. Meksiarun, P. H. B. Aoki, S. J. Van Nest, R. G. Sobral-Filho, J. J. Lum, A. G. Brolo and A. Jirasek, *Analyst*, 2018, **143**, 3850-3858.
17. D. Lazaro-Pacheco, A. M. Shaaban, N. A. Titiloye, S. Rehman and I. U. Rehman, *EXCLI J*, 2021, **20**, 1118-1132.

18. R. Vanna, C. Morasso, B. Marcinnò, F. Piccotti, E. Torti, D. Altamura, S. Albasini, M. Agozzino, L. Villani, L. Sorrentino, O. Bunk, F. Leporati, C. Giannini and F. Corsi, *Cancer Research*, 2020, **80**, 1762-1772.
19. S. J. Van Nest, L. M. Nicholson, L. DeVorkin, A. G. Brolo, J. J. Lum and A. Jirasek, *Radiation Research*, 2018, **189**, 497-504.
20. H. Abramczyk, J. M. Surmacki and B. Brozek-Pluska, *Journal of Molecular Structure*, 2022, **1252**, 132134.
21. X. Wen, Y.-C. Ou, G. Bogatcheva, G. Thomas, A. Mahadevan-Jansen, B. Singh, E. C. Lin and R. Bardhan, *Chemical Science*, 2020, **11**, 9863-9874.
22. X. Bi, B. Rexer, C. Arteaga, M. Guo and A. Mahadevan-Jansen, *Journal of Biomedical Optics*, 2014, **19**, 025001.
23. L. Hartsuiker, N. J. L. Zeijen, L. W. M. M. Terstappen and C. Otto, *Analyst*, 2010, **135**, 3220-3226.
24. L. Zhang, C. Li, D. Peng, X. Yi, S. He, F. Liu, X. Zheng, W. E. Huang, L. Zhao and X. Huang, *Spectrochimica Acta Part A: Molecular and Biomolecular Spectroscopy*, 2022, **264**, 120300.
25. C. Nieva, M. Marro, N. Santana-Codina, S. Rao, D. Petrov and A. Sierra, *PLOS ONE*, 2012, **7**, e46456.
26. A. C. S. Talari, C. A. Evans, I. Holen, R. E. Coleman and I. U. Rehman, *Journal of Raman Spectroscopy*, 2015, **46**, 421-427.
27. L. T. Kerr, H. J. Byrne and B. M. Hennelly, *Analytical Methods*, 2015, **7**, 5041-5052.
28. A. T. Lewis, R. Gaifulina, M. Isabelle, J. Dorney, M. L. Woods, G. R. Lloyd, K. Lau, M. Rodriguez-Justo, C. Kendall, N. Stone and G. M. Thomas, *Journal of Raman Spectroscopy*, 2017, **48**, 119-125.
29. M. Gellner, B. Küstner and S. Schlücker, *Vibrational Spectroscopy*, 2009, **50**, 43-47.
30. X. X. Han, R. S. Rodriguez, C. L. Haynes, Y. Ozaki and B. Zhao, *Nature Reviews Methods Primers*, 2022, **1**, 87.
31. A. J. Hobro and N. I. Smith, *Vibrational Spectroscopy*, 2017, **91**, 31-45.
32. E. Toijer and M. Jonsson, *Radiation Physics and Chemistry*, 2019, **159**, 159-165.
33. M. R. Raychaudhuri and P. Brimblecombe, *Studies in Conservation*, 2000, **45**, 226-232.
34. M. Ai, *Journal of Catalysis*, 1983, **83**, 141-150.
35. T. Yumura, T. Amenomori, Y. Kagawa and K. Yoshizawa, *The Journal of Physical Chemistry A*, 2002, **106**, 621-630.

36. C.-H. Tseng, J. F. Ford, C. K. Mann and T. J. Vickers, *Applied Spectroscopy*, 1993, **47**, 1808-1813.
37. H. O. Hamaguchi, *Applied Spectroscopy Reviews*, 1988, **24**, 137-174.
38. R. Gautam, D. Peoples, K. Jansen, M. O'Connor, G. Thomas, S. Vanga, I. J. Pence and A. Mahadevan-Jansen, *Appl. Spectrosc.*, 2020, **74**, 1238-1251.
39. X.-g. Fan, Y. Zeng, Y.-L. Zhi, T. Nie, Y.-j. Xu and X. Wang, *Journal of Raman Spectroscopy*, 2021, **52**, 890-900.
40. M. Esteki, Z. Shahsavari and J. Simal-Gandara, *Food Control*, 2018, **91**, 100-112.
41. X. Li, Q. Wang, F. Nie and M. Chen, *IEEE Transactions on Cybernetics*, 2021, DOI: 10.1109/TCYB.2021.3049684, 1-12.
42. W. R. Adams, B. Mehl, E. Lieser, M. Wang, S. Patton, G. A. Throckmorton, J. L. Jenkins, J. B. Ford, R. Gautam, J. Brooker, E. D. Jansen and A. Mahadevan-Jansen, *Scientific Reports*, 2021, **11**, 8067.
43. S. Balakrishnama and A. Ganapathiraju, *Institute for Signal and information Processing*, 1998, **18**, 1-8.
44. C. A. Jenkins, R. A. Jenkins, M. M. Pryse, K. A. Welsby, M. Jitsumura, C. A. Thornton, P. R. Dunstan and D. A. Harris, *Analyst*, 2018, **143**, 6014-6024.
45. S. J. Barton, K. O'Dwyer, M. Butler, A. Dignam, H. J. Byrne, L. O'Neill and B. M. Hennelly, *Analytical Methods*, 2019, **11**, 6023-6032.
46. K. Anselme, B. Noe¨l and P. Hardouin, *Journal of Materials Science: Materials in Medicine*, 1999, **10**, 815-819.
47. L. Hao, J. Lawrence, Y. F. Phua, K. S. Chian, G. C. Lim and H. Y. Zheng, *Journal of Biomedical Materials Research Part B: Applied Biomaterials*, 2005, **73B**, 148-156.
48. S. Ni, L. Sun, B. Ercan, L. Liu, K. Ziemer and T. J. Webster, *Journal of Biomedical Materials Research Part B: Applied Biomaterials*, 2014, **102**, 1297-1303.
49. A. G. Ryder, J. D. Vincentis, B. Li, P. W. Ryan, N. M. S. Sirimuthu and K. J. Leister, *Journal of Raman Spectroscopy*, 2010, **41**, 1266-1275.
50. L. Mikoliunaite, R. D. Rodriguez, E. Sheremet, V. Kolchuzhin, J. Mehner, A. Ramanavicius and D. R. T. Zahn, *Scientific Reports*, 2015, **5**, 13150.
51. K. Esmonde-White, M. Lewis, T. Perilli, T. Della Vedova and I. Lewis, 2022, **37**, 34–45.
52. K. Czamara, K. Majzner, M. Z. Pacia, K. Kochan, A. Kaczor and M. Baranska, *Journal of Raman Spectroscopy*, 2015, **46**, 4-20.
53. R. Manoharan, J. J. Baraga, M. S. Feld and R. P. Rava, *Journal of Photochemistry and Photobiology B: Biology*, 1992, **16**, 211-233.

54. L. E. Jamieson, A. Li, K. Faulds and D. Graham, *Royal Society Open Science*, 2018, **5**, 181483.
55. L. Cui, H. J. Butler, P. L. Martin-Hirsch and F. L. Martin, *Analytical Methods*, 2016, **8**, 481-487.
56. F. Ligorio, I. Pellegrini, L. Castagnoli, A. Vingiani, R. Lobefaro, E. Zattarin, M. Santamaria, S. M. Pupa, G. Pruneri, F. de Braud and C. Vernieri, *Cancer Letters*, 2021, **511**, 77-87.
57. S. Kim, Y. Lee and J. S. Koo, *PLOS ONE*, 2015, **10**, e0119473.
58. A. Vazquez-Martin, R. Colomer, J. Brunet, R. Lupu and J. A. Menendez, *Cell Proliferation*, 2008, **41**, 59-85.
59. C. Rodrigues, L. Milkovic, I. T. Bujak, M. Tomljanovic, G. Soveral and A. Cipak Gasparovic, *Oxidative Medicine and Cellular Longevity*, 2019, **2019**, 2061830.
60. T. J. Kochel, O. G. Goloubeva and A. M. Fulton, *Breast Cancer: Basic and Clinical Research*, 2016, **10**, BCBCR.S38529.
61. K. Mosalpuria, C. Hall, S. Krishnamurthy, A. Lodhi, D. M. Hallman, M. S. Baraniuk, A. Bhattacharyya and A. Lucci, *Mol Clin Oncol*, 2014, **2**, 845-850.
62. J. Tian, M. Y. Hachim, I. Y. Hachim, M. Dai, C. Lo, F. A. Raffa, S. Ali and J. J. Lebrun, *Scientific Reports*, 2017, **7**, 40258.
63. M. E. Reyes, PhD, The University of Texas Graduate School of Biomedicial Sciences, 2014.
64. Z. M. Abgarmi, A. S. Lotfi, S. Abroun, M. Soleimani, S. M. Ganji, P. Baktash and A. Moradi, *Archives of Breast Cancer*, 2021, 137-142.
65. R. W. Holloway and P. A. Marignani, *Cancers*, 2021, **13**, 2922.
66. E. Shin and J. S. Koo, *Frontiers in Cell and Developmental Biology*, 2021, **9**.
67. Y. R. Hussein, S. Bandyopadhyay, A. Semaan, Q. Ahmed, B. Albashiti, T. Jazaerly, Z. Nahleh and R. Ali-Fehmi, *Translational Oncology*, 2011, **4**, 321-327.
68. S. Alexandrou, S. M. George, C. J. Ormandy, E. Lim, S. R. Oakes and C. E. Caldon, *International Journal of Molecular Sciences*, 2019, **20**, 667.
69. Z. Movasaghi, S. Rehman and I. U. Rehman, *Applied Spectroscopy Reviews*, 2007, **42**, 493-541.
70. C. Krafft, L. Neudert, T. Simat and R. Salzer, *Spectrochimica Acta Part A: Molecular and Biomolecular Spectroscopy*, 2005, **61**, 1529-1535.
71. R. Gautam, S. Vanga, A. Madan, N. Gayathri, U. Nongthomba and S. Umapathy, *Analytical Chemistry*, 2015, **87**, 2187-2194.
72. A. Dutta, R. Gautam, S. Chatterjee, F. Ariese, S. K. Sikdar and S. Umapathy, *ACS Chemical Neuroscience*, 2015, **6**, 1794-1801.

73. J. W. Chan, D. S. Taylor, T. Zwerdling, S. M. Lane, K. Ihara and T. Huser, *Biophys J*, 2006, **90**, 648-656.
74. N. Stone, C. Kendall, J. Smith, P. Crow and H. Barr, *Faraday Discussions*, 2004, **126**, 141-157.
75. S. Koljenović, T. B. Schut, A. Vincent, J. M. Kros and G. J. Puppels, *Analytical Chemistry*, 2005, **77**, 7958-7965.

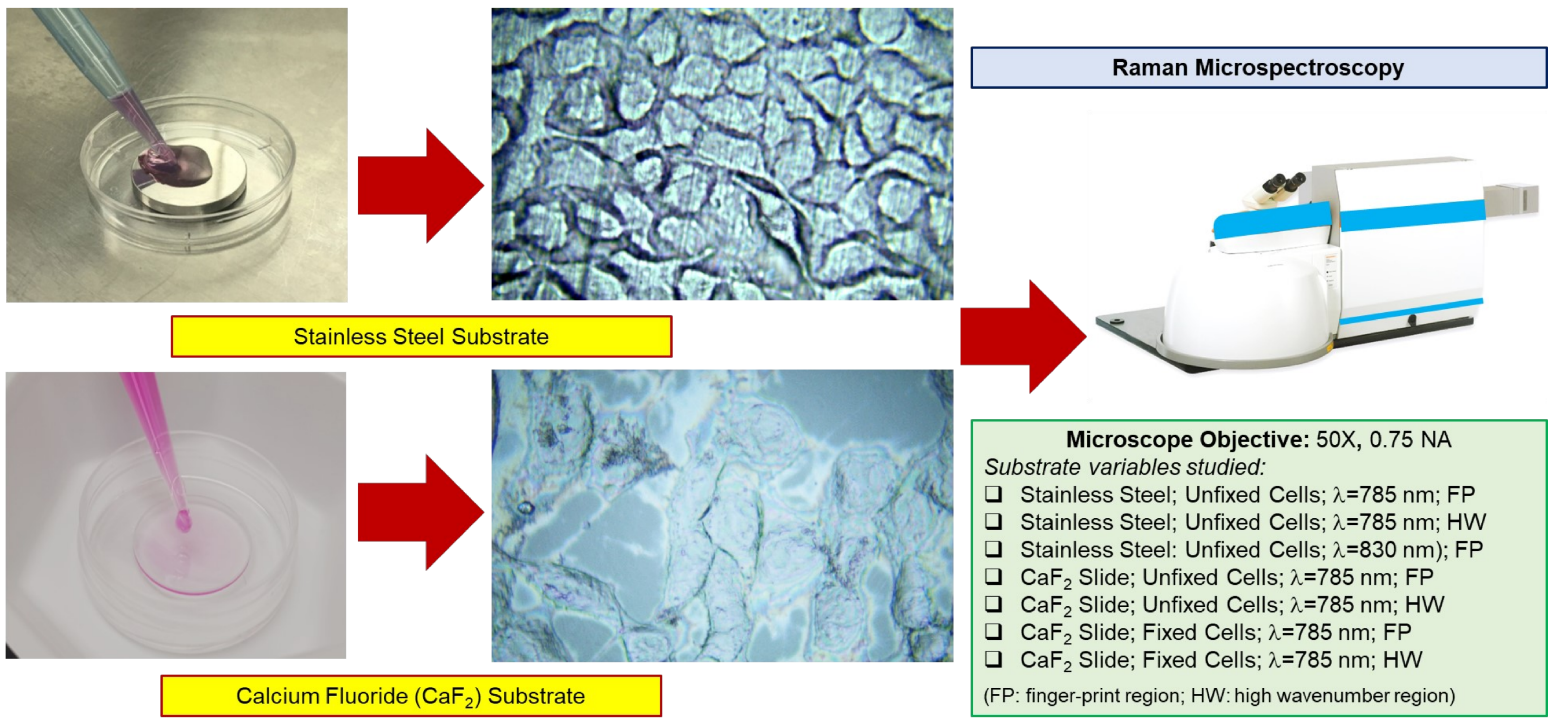

Figure 1: Methodology adopted to compare Raman signal obtained on stainless steel versus calcium fluoride (CaF_2) substrate for breast cancer cells. Influence of the following variables on Raman signal-to-noise ratio (SNR) was considered – laser wavelength (785 or 830 nm), laser power (0.055 – 5.5 mW) and use of fixative (4% paraformaldehyde in phosphate-buffered saline).

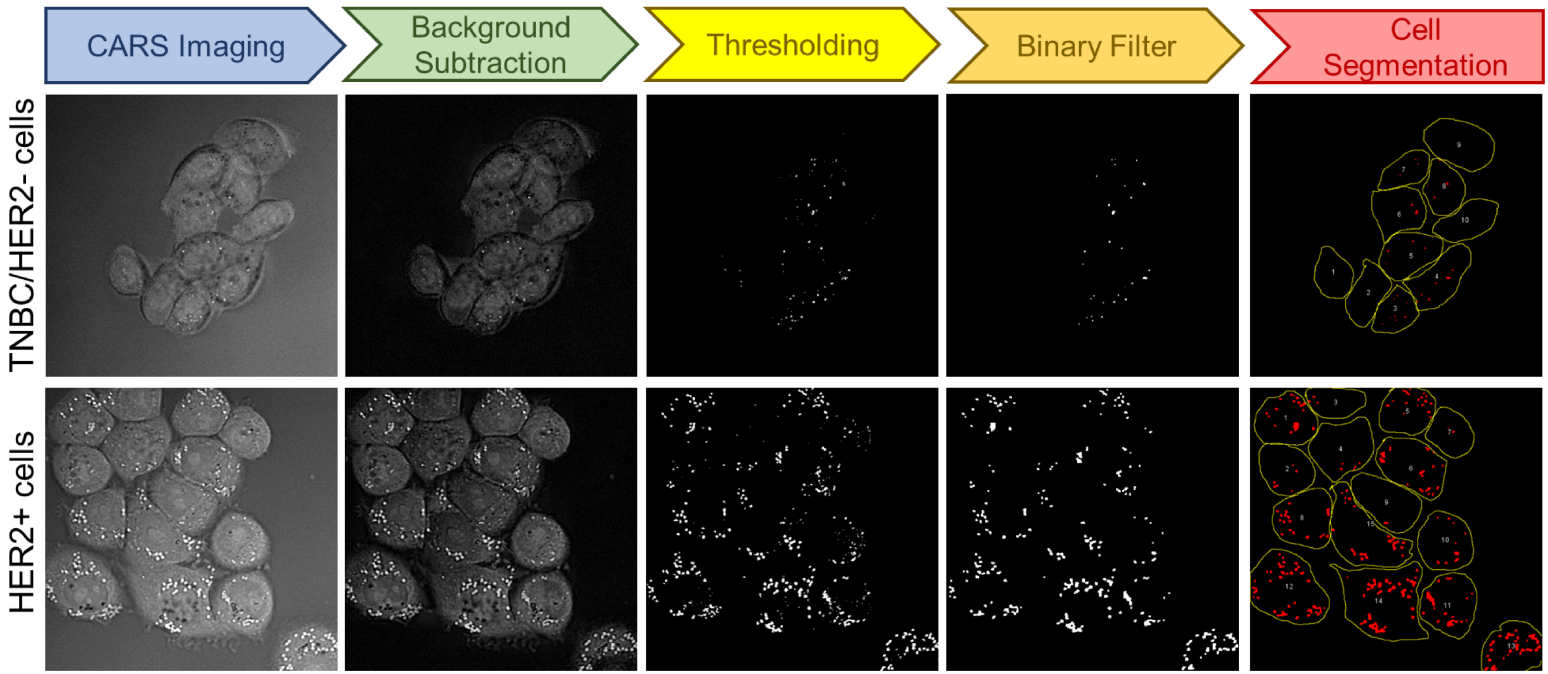

Figure 2: Illustration of the image processing workflow adopted to quantify the percentage of cell area covered by lipid droplets. Quantification was performed on images obtained from various breast cancer cells (HER2+ and TNBC/HER2- cells) using coherent anti-Stokes Raman scattering (CARS) microscopy that was performed at 2850 cm^{-1}, which is conventionally assigned to CH_2 symmetric stretch in lipids.

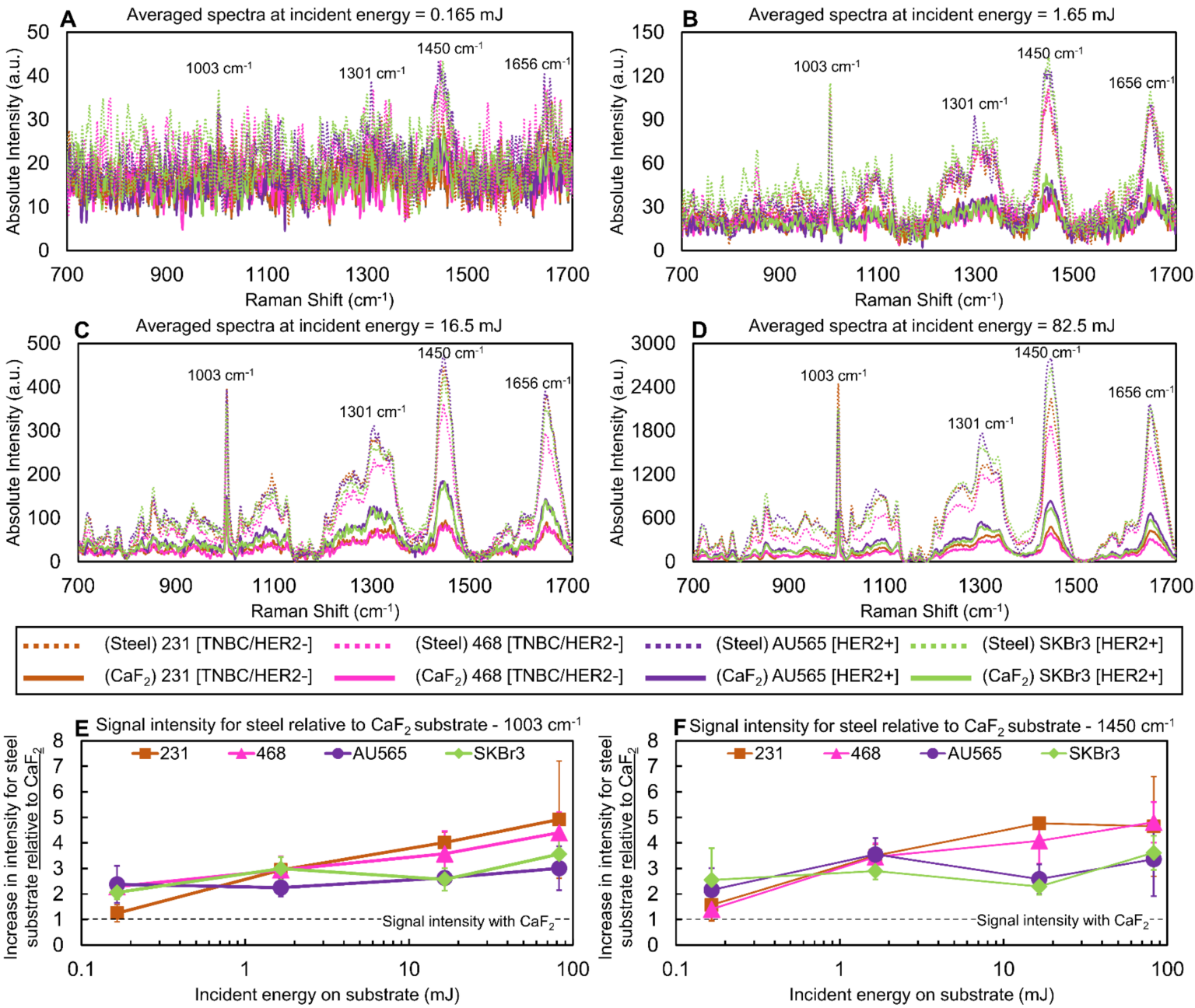

Figure 3: Comparison of Raman signal intensity in the fingerprint wavenumber region for breast cancer cells grown on stainless steel versus calcium fluoride (CaF_2) substrate. (**A – D**) Signal intensity of averaged Raman spectra was compared for incident energy that ranged from 0.165 to 82.5 mJ. Raman signal intensity was amplified on stainless steel compared to CaF_2 substrate for all four cell lines. The absolute Raman signal intensity of HER2+ cells (AU565, SKBr3) was greater than TNBC/HER2- cells (231, 468) on both stainless steel and CaF_2 substrates. (**E – F**) The amplification of Raman signal on stainless steel relative to CaF_2 substrate was more pronounced for TNBC/HER2- cells when quantified at 1003 cm^{-1} and 1450 cm^{-1}, which served as the landmark wavenumbers for the fingerprint region. The slope of Raman signal increase/amplification on stainless steel relative to CaF_2 intensity was more pronounced for TNBC/HER2- cells than HER2+ cells, especially above an incident energy of 1.65 mJ. The error bars denote the standard deviation of the quantified values denoted in the plot.

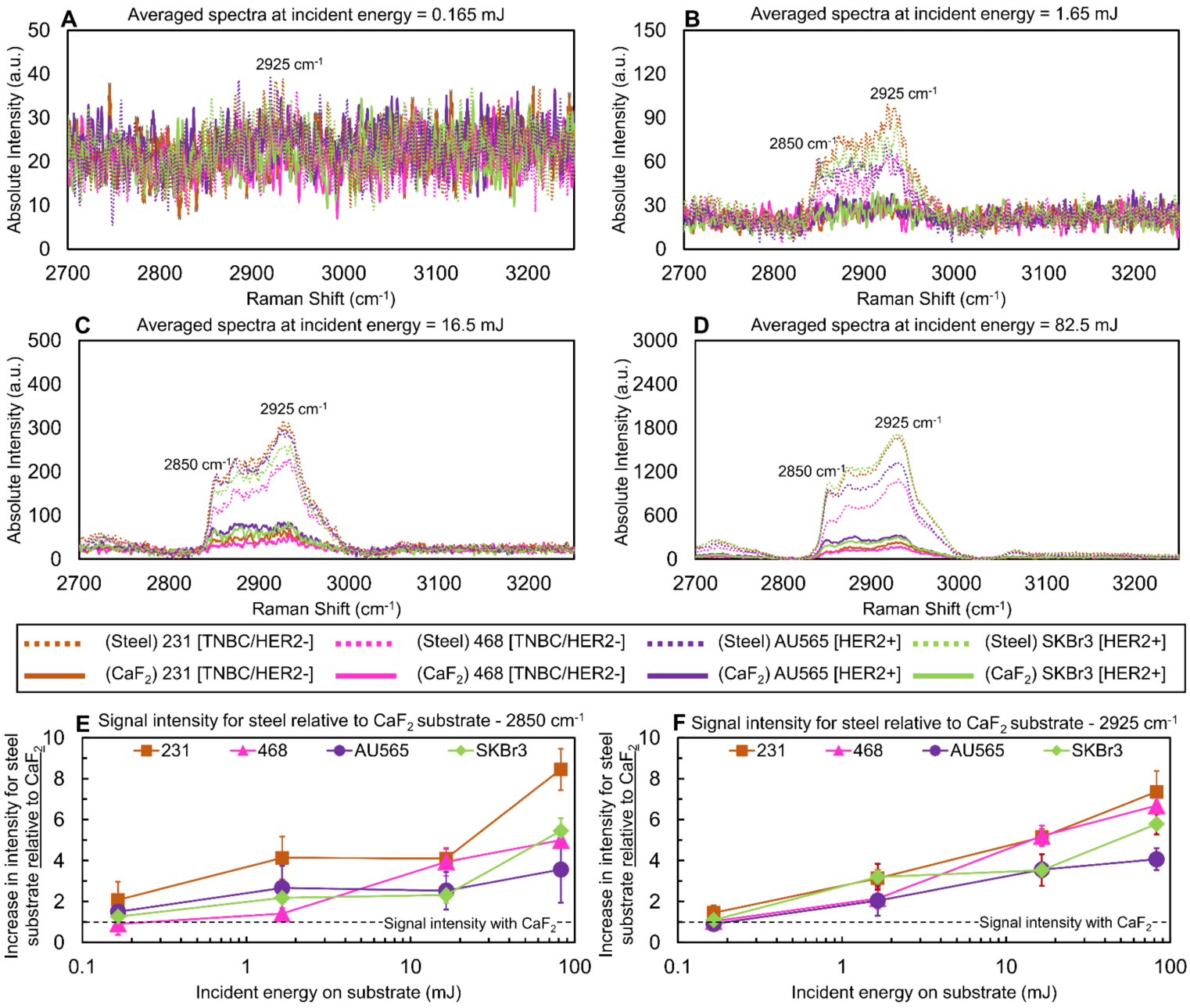

Figure 4: Comparison of Raman signal intensity in the high wavenumber region for breast cancer cells grown on stainless steel versus calcium fluoride (CaF_2) substrate. (**A – D**) Signal intensity of averaged Raman spectra was compared for incident energy that ranged 0.165 to 82.5 mJ. Raman signal intensity was amplified on stainless steel compared to CaF_2 substrate for all four cell lines. The absolute Raman signal intensity of HER2+ cells (AU565, SKBr3) was greater than TNBC/HER2- cells (231, 468) on both stainless steel and CaF_2 substrates. (**E – F**) The amplification of Raman signal on stainless steel relative to CaF_2 substrate was more pronounced for TNBC/HER2- cells when quantified at 2850 cm^{-1} and 2925 cm^{-1}, which served as the landmark wavenumbers for the high wavenumber region. The slope of Raman signal increase/amplification on stainless steel relative to CaF_2 intensity was more pronounced for TNBC/HER2- cells than HER2+ cells, especially above an incident energy of 1.65 mJ. The error bars denote the standard deviation of the quantified values denoted in the plot.

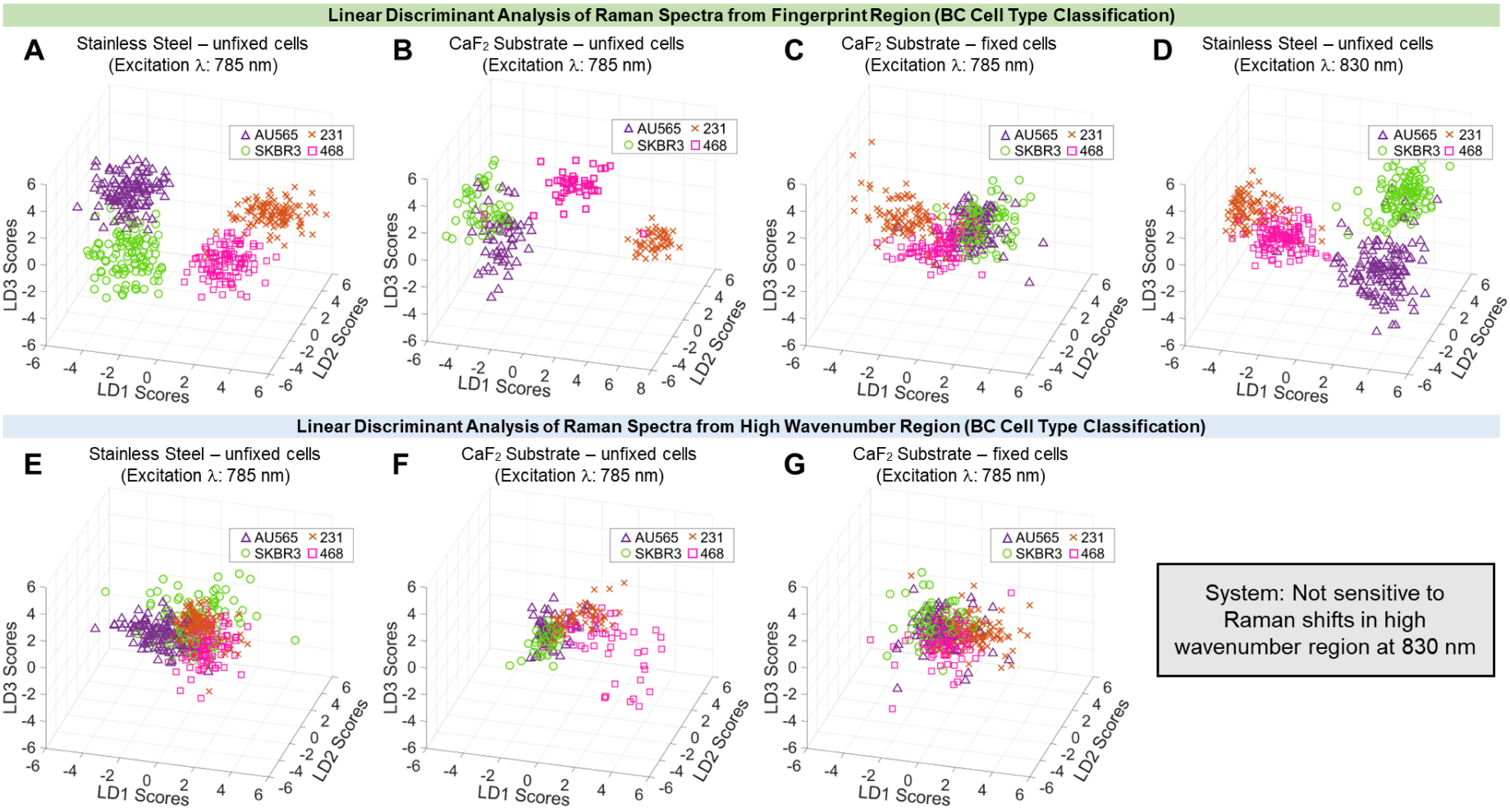

Figure 5: Linear discriminant analysis (LDA) of the Raman spectra from breast cancer cells based on cell type. Separation was superior in the fingerprint region (**A – D**) compared to the high wavenumber region (**E – G**). LDA classification for all four cell lines based on cell type appears to be superior for Raman spectra obtained on unfixed cells grown on stainless steel with (**A**) 785 nm excitation and (**D**) 830 nm excitation, compared to those from (**B**) unfixed cells on CaF_2 substrate at 785 nm excitation [See accuracy measured from confusion matrices in **Figure 6**]. Separation for the four cell types with LDA were the poorest for fixed cells on CaF_2 substrate for both (**C**) fingerprint region and (**G**) high wavenumber region.

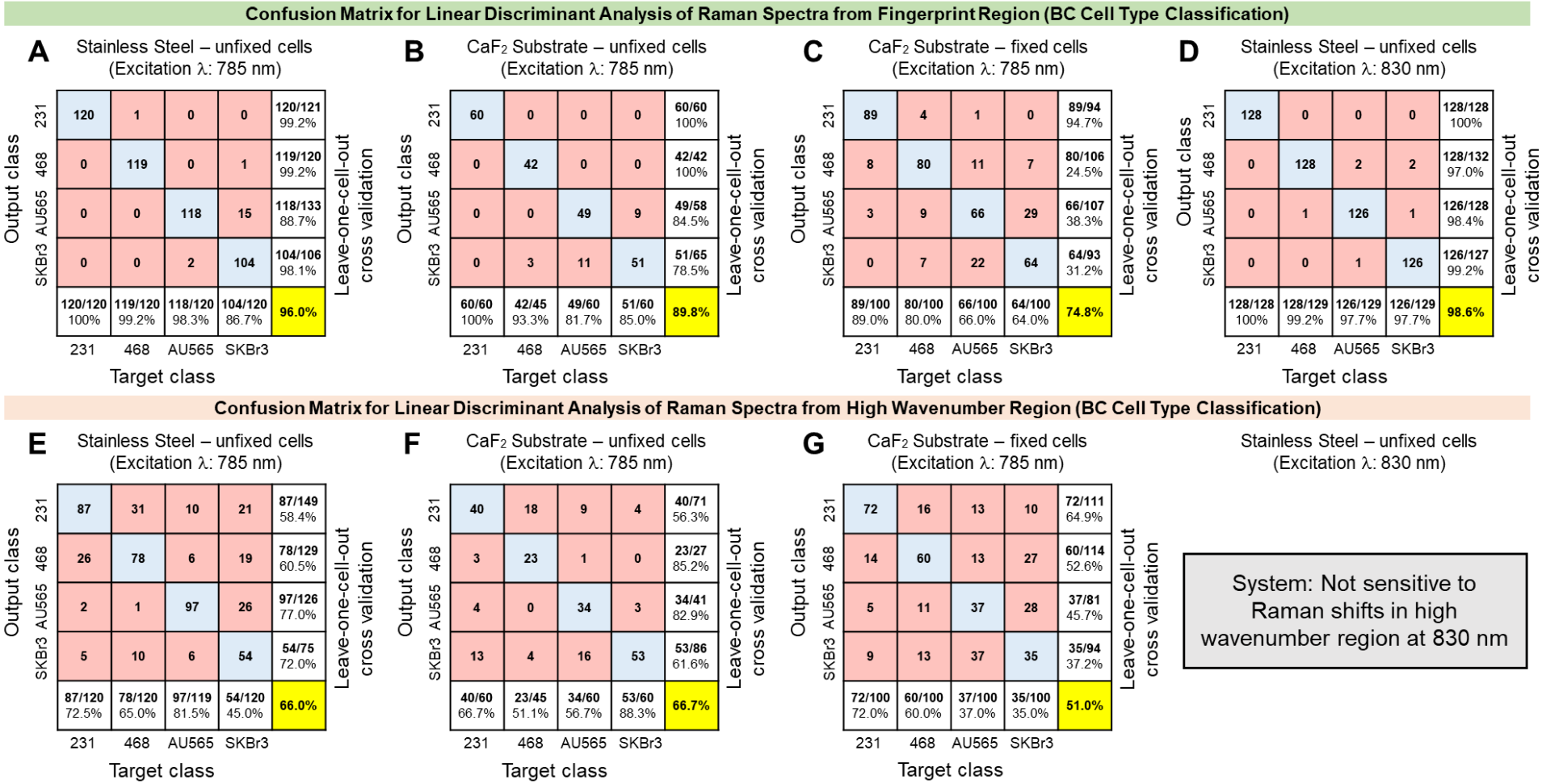

Figure 6: Confusion matrices denoting the accuracies based on linear discriminant analysis (LDA) depicted in **Figure 5**. Classification accuracies for breast cancer cells based on cell type was highest at 74.8% - 98.6% in the fingerprint region (**A – D**) compared to 51% - 66.7% for the high wavenumber region (**E – G**). LDA classification for all four cell types appears to be the highest for unfixed cells grown on stainless steel with (**A**) 785 nm excitation at 96% and (**D**) 830 nm excitation at 98.6%, compared to those from (**B**) unfixed cells on CaF_2 substrate at 785 nm excitation at 89.8%. Classification accuracy based on cell types was the poorest for fixed cells on CaF_2 substrate for both (**C**) fingerprint region at 74.8% and (**G**) high wavenumber region at 51%.

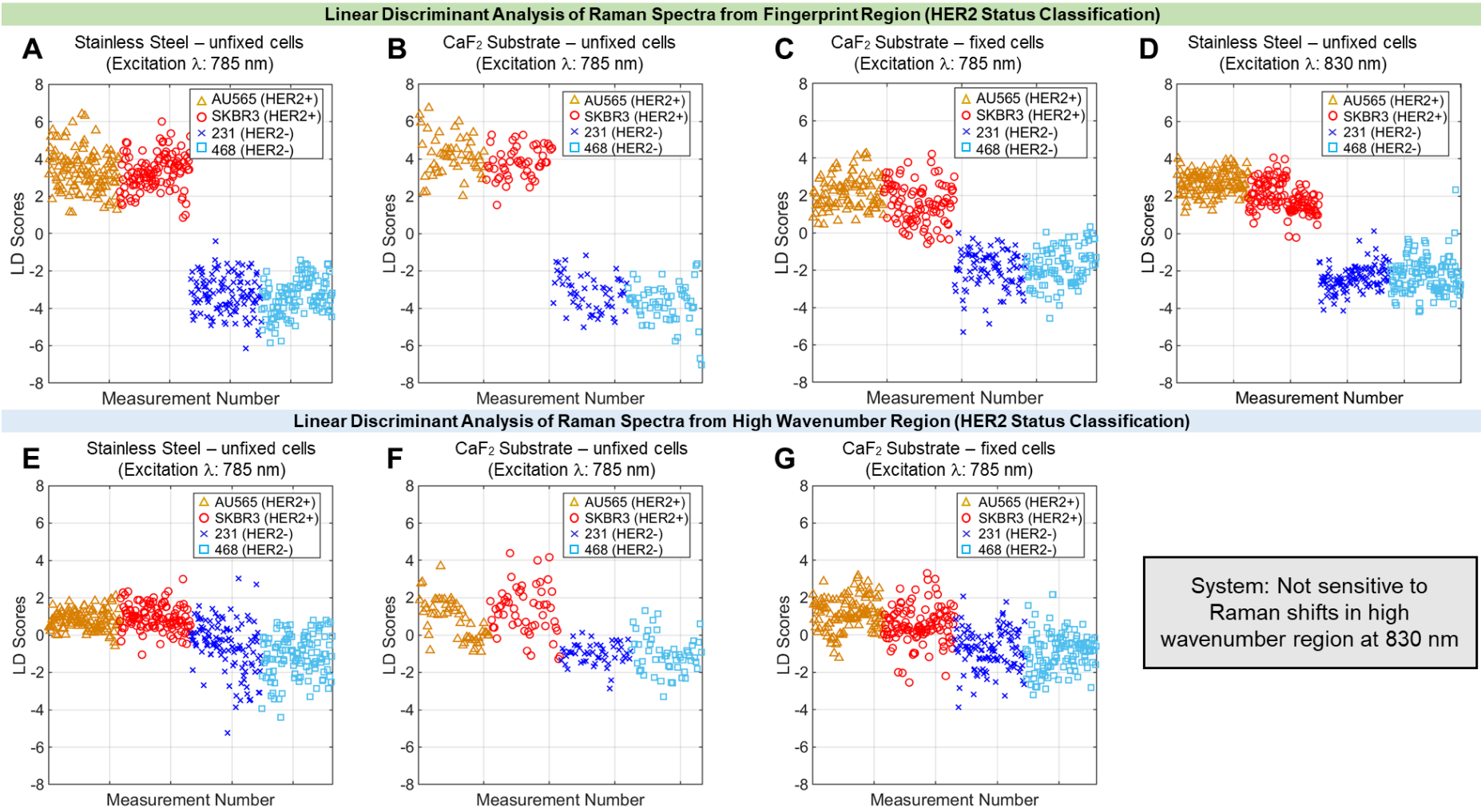

Figure 7: Linear discriminant analysis (LDA) of the Raman spectra from breast cancer cells based on HER2 expression status. Separation based on HER2 status was observed to be superior in the fingerprint region (**A – D**) compared to the high wavenumber region (**E – G**). LDA classification based on HER2 status was comparable across Raman spectra obtained on (**A**) unfixed cells on stainless steel, (**B**) unfixed cells on CaF_2 substrate at 785 nm excitation and (**D**) unfixed cells on stainless steel at 830 nm excitation [See accuracy measured from confusion matrices in **Figure 8**]. Separation for cells based on HER2 status with LDA was the poorest for fixed cells on CaF_2 substrate for both (**C**) fingerprint region and (**G**) high wavenumber region.

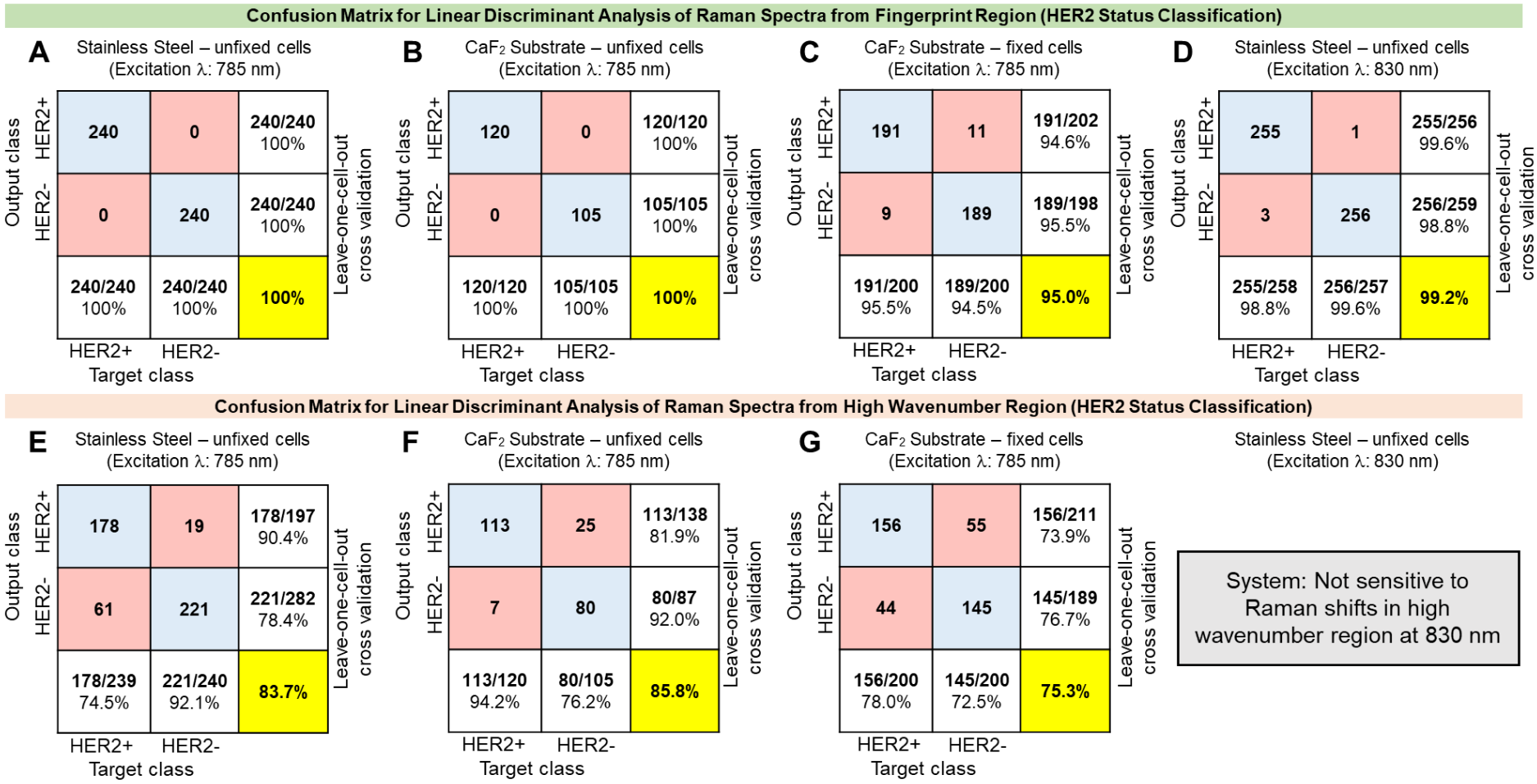

Figure 8: Confusion matrices denoting the accuracies based on linear discriminant analysis (LDA) depicted in **Figure 7**. Classification accuracies for breast cancer cells based on HER2 status were higher at 95% - 100% in the fingerprint region (**A – D**) compared to 75.3% - 85.8% for the high wavenumber region (**E – G**). Classification accuracy based on HER2 status was comparable across Raman spectra obtained on (**A**) unfixed cells on stainless steel at 100%, (**B**) unfixed cells on CaF_2 substrate at 785 nm excitation at 100% and (**D**) unfixed cells on stainless steel at 830 nm excitation at 99.2%. Classification accuracy for Raman spectra based on HER2 status was lower for fixed cells on CaF_2 substrate for both (**C**) fingerprint region at 95% and (**G**) high wavenumber region at 75.3%.

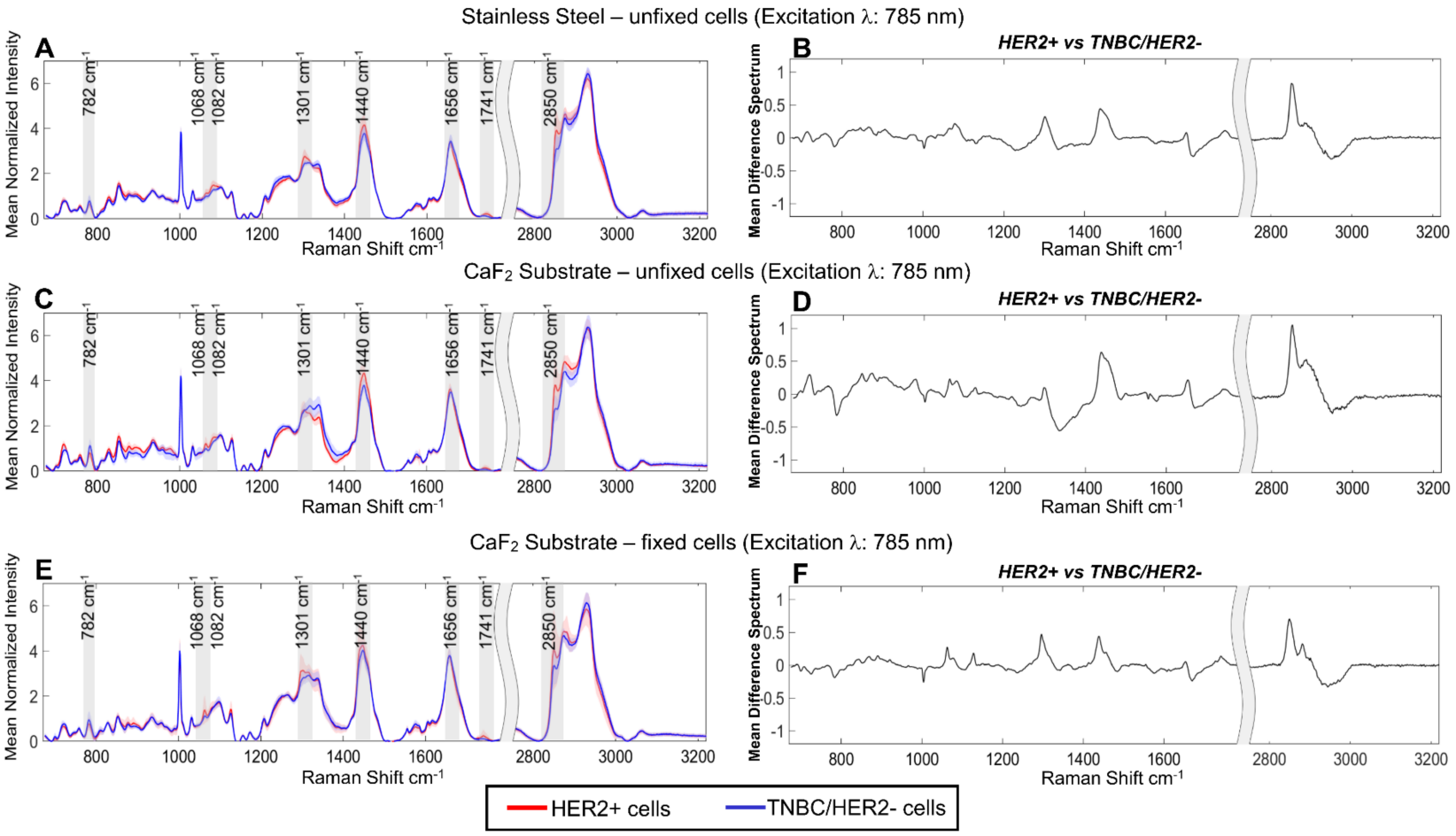

Figure 9: Comparison of averaged mean normalized Raman spectra from unfixed HER2+ cells (red) and TNBC/HER2- cells (blue) grown on (**A**) stainless steel and (**B**) corresponding mean difference spectrum between the two groups of cells. Similarly, a comparison of Raman spectra between the two groups of breast cancer cells have been denoted for (**C** & **D**) for unfixed cells grown on CaF_2 substrate and (**E** & **F**) for fixed cells grown on CaF_2 substrate. The excitation source for the averaged mean normalized spectra depicted in (**A**, **C** and **E**) was 785 nm. Across all three experimental variables, HER2+ cells consistently exhibited stronger intensity at 1068-1082 cm^{-1}, 1301 cm^{-1},1440 cm^{-1},1741 cm^{-1} and 2850 cm^{-1}, while TNBC/HER2- yielded stronger intensity at 782 cm^{-1} and 1656 cm^{-1}. These spectral differences are denoted by the grey shaded boxes and have been further highlighted in the mean difference spectrum between HER2+ and TNBC/HER2- cells depicted in **B**, **D** and **F**. Light red shaded and light blue shaded region in **A**, **C** and **E** denote the standard error for the averaged mean normalized Raman spectra for HER2+ and TNBC/HER2- cells respectively.

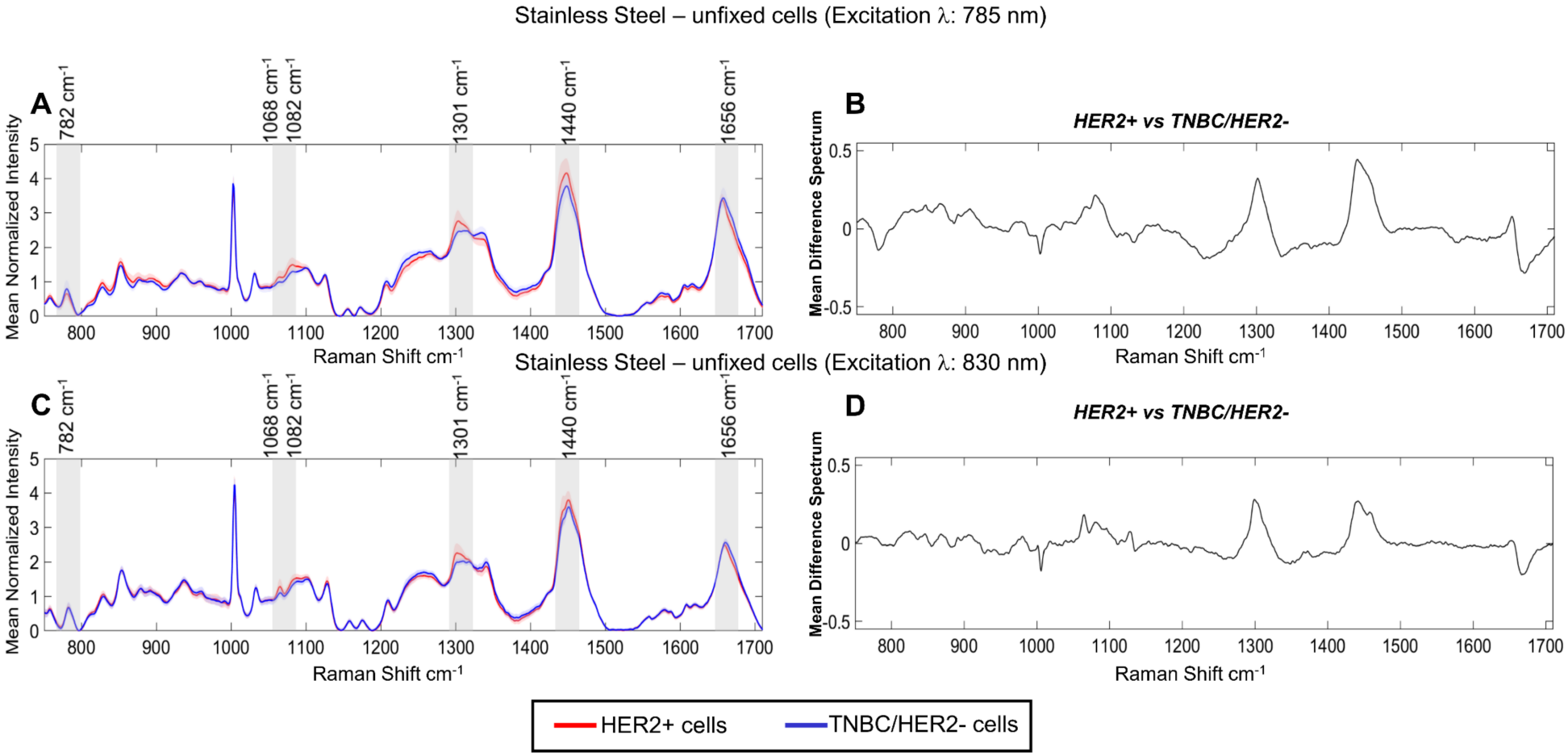

Figure 10: Comparison of averaged mean normalized Raman spectra from unfixed HER2+ cells (red) and TNBC/HER2- cells (blue) grown on (**A**) stainless steel at 785 nm excitation and (**B**) corresponding mean difference spectrum between the two groups of cells. Similarly, a comparison of Raman spectra between the two groups of breast cancer cells has been denoted for (**C** & **D**) for unfixed cells grown on stainless steel at 830 nm excitation. Under both excitation wavelengths, HER2+ cells consistently exhibited stronger intensity at 1068-1082 cm^{-1}, 1301 cm^{-1} and 1440 cm^{-1}, while TNBC/HER2- yielded stronger intensity at 782 cm^{-1} and 1656 cm^{-1}. These spectral differences are denoted by the grey shaded boxes and have been further highlighted in the mean difference spectrum between HER2+ and TNBC/HER2- cells depicted in **B** and **D**. Light red shaded and light blue shaded region in **A** and **C** denote the standard error for the averaged mean normalized Raman spectra.

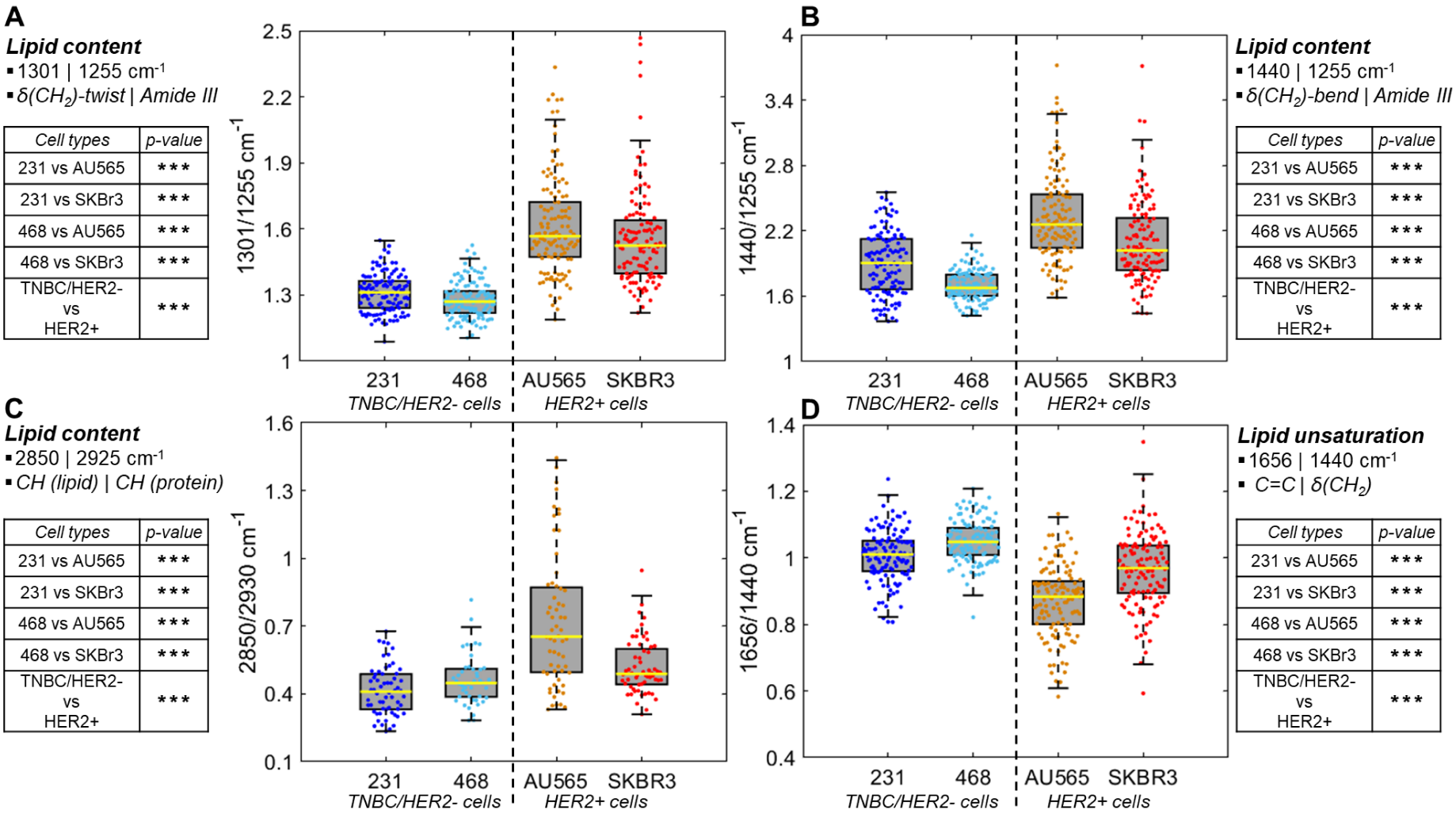

Figure 11: Ratio-metric analysis of lipid dominant peaks from Raman spectral data obtained from breast cancer cells grown on stainless steel. (**A**, **B** & **C**) HER2+ breast cancer cells yielded significantly higher spectral ratios (1301/1255 cm^{-1}, 1440/1255 cm^{-1} and 2850/2925 cm^{-1}) that indicate an increase in lipids relative to proteins, when compared to TNBC/HER2- cells (***, p<0.001). (**D**) TNBC/HER2- cells demonstrated higher values for the 1656/1400 cm^{-1} ratio than HER2+ cells, suggesting a rise in unsaturated lipids relative to the total amount of lipids within the cancer cells (***, p <0.001). The yellow line in the box plots represents the median value for each group, while the bottom and top edges of the box indicate the 25th and 75th percentiles, respectively. The bars of the box plot extend to the most extreme data points not considered outliers, and the outliers are plotted individually beyond the whisker bars.

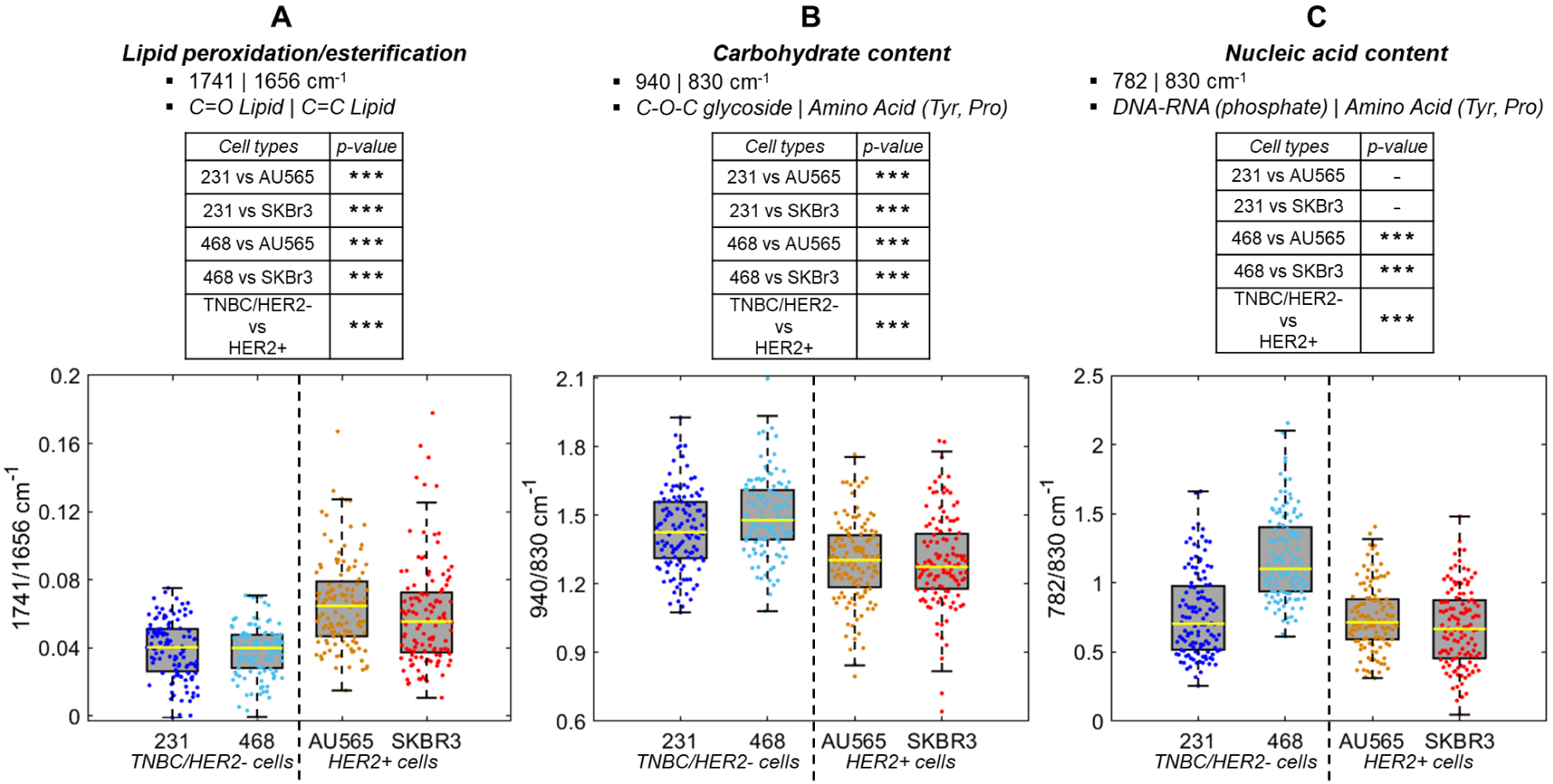

Figure 12: Ratio-metric analysis of peaks pertaining to lipid peroxidation, carbohydrate and nucleic acid content from Raman spectral data obtained from breast cancer cells grown on stainless steel. (**A**) HER2+ breast cancer cells provided higher spectral ratios at 1741/1656 cm^{-1} suggesting a higher degree of lipid peroxidation, when compared to TNBC/HER2- cells (***, p<0.001). (**B**) TNBC/HER2- cells yielded a notable rise for the 946/830 cm^{-1} ratio compared to HER2+ cells, indicating increased presence of carbohydrates relative to amino acids for these cells (***, p <0.001). (**C**) The 782/830 cm^{-1} ratio was the most prominently elevated for MDA-MB-468 (denoted here as '468', TNBC basal-type, HER2-) compared to the other breast cancer cells, signifying a significant increase of nucleic acid content in these cells compared to the remaining three cells (***, p<0.001). The yellow line in the box plots represent the median value for each group, while the bottom and top edges of the box indicate the 25th and 75th percentiles, respectively. The bars of the box plot extend to the most extreme data points not considered outliers, and the outliers are plotted individually beyond the whisker bars.

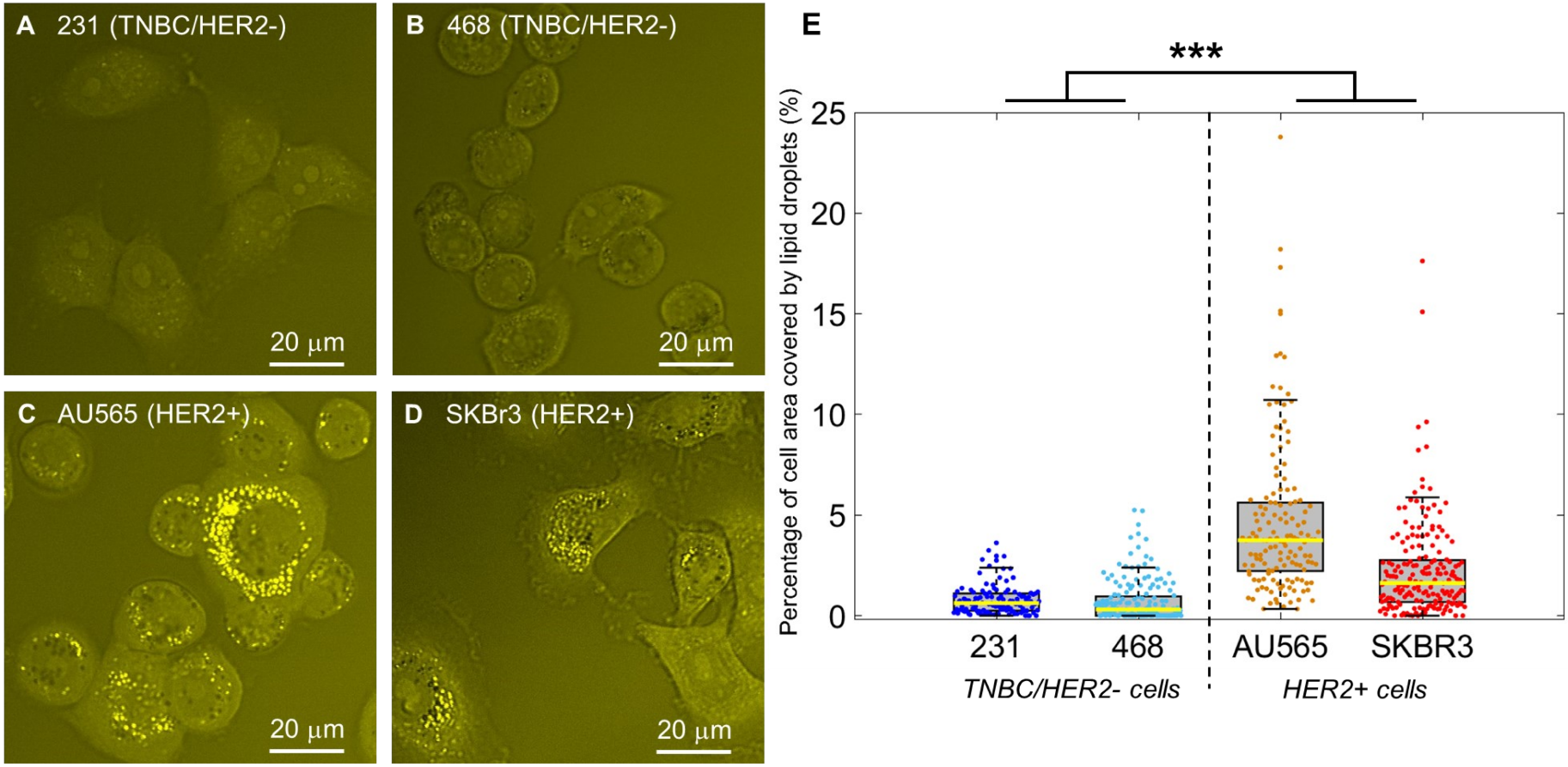

Figure 13: (**A – D**) Coherent anti-Stokes Raman Scattering (CARS) microscopy images of breast cancer cells obtained at 2850 cm^{-1} that is conventionally assigned to CH_2 symmetric stretch in lipids. The CARS images suggest the increased presence of lipid content (e.g., intracellular lipid droplets) in (**C** & **D**) HER2+ cells compared to (**A** & **B**) TNBC/HER2- cells. (**E**) Box plot quantifying the percentage of cell area occupied by lipid droplets using the schematic described in **Figure 2**. In HER2+ cells, the area covered with lipid droplets was about 2.5 – 4 times more than TNBC/HER2- cells ($p<0.001$). The yellow line in the box plots represents the median value for each group, while the bottom and top edges of the box indicate the 25th and 75th percentiles, respectively. The bars of the box plot extend to the most extreme data points not considered outliers, and the outliers are plotted individually beyond the whisker bars.